



HAL
open science

Evaluating and Validating 3D Simulated MASW and SPAC In-Situ Tests in Argostoli, Greece

Andrea Riaño, Fernando Lopez-caballero, Fabrice Hollender

► **To cite this version:**

Andrea Riaño, Fernando Lopez-caballero, Fabrice Hollender. Evaluating and Validating 3D Simulated MASW and SPAC In-Situ Tests in Argostoli, Greece. *Geophysical Journal International*, 2024, 238 (2), pp.1053-1072. 10.1093/gji/ggae187. hal-04599501

HAL Id: hal-04599501

<https://hal.science/hal-04599501>

Submitted on 28 Jun 2024

HAL is a multi-disciplinary open access archive for the deposit and dissemination of scientific research documents, whether they are published or not. The documents may come from teaching and research institutions in France or abroad, or from public or private research centers.

L'archive ouverte pluridisciplinaire **HAL**, est destinée au dépôt et à la diffusion de documents scientifiques de niveau recherche, publiés ou non, émanant des établissements d'enseignement et de recherche français ou étrangers, des laboratoires publics ou privés.



Distributed under a Creative Commons Attribution 4.0 International License

Evaluating and validating 3-D simulated MASW and SPAC *in situ* tests in Argostoli, Greece

Andrea C. Riaño¹,¹ Fernando Lopez-Caballero¹ and Fabrice Hollender^{2,3}

¹Laboratoire de Mécanique Paris-Saclay (LMPS) CNRS UMR-9026, Université Paris-Saclay, CentraleSupélec, École Normale Supérieure, 91192 Gif-sur-Yvette, France. E-mail: ac.riano384@univ-paris-saclay.fr

²French Alternative Energies and Atomic Energy Commission (CEA), DES, CEA Cadarache, 13108 Saint Paul Lez Durance, France.

³University Grenoble Alpes, University Savoie Mont Blanc, CNRS, IRD, University Gustave Eiffel, ISTerre, 38058 Grenoble, France.

Accepted 2024 May 14. Received 2024 May 10; in original form 2023 September 21

SUMMARY

Geophysics and Geotechnical Engineering commonly use 1-D wave propagation analysis, simplifying complex scenarios by assuming flat and homogeneous soil layers, vertical seismic wave propagation and negligible pore water pressure effects (total stress analysis). These assumptions are commonly used in practice, providing the basis for applications like analysing site responses to earthquakes and characterizing soil properties through inversion processes. These processes involve various *in situ* tests to estimate the subsurface soil's material profile, providing insights into its behaviour during seismic events. This study seeks to address the limitations inherent to 1-D analyses by using 3-D physics-based simulations to replicate *in situ* tests performed in the Argostoli basin, Greece. Active and passive source surveys are simulated, and their results are used to determine material properties at specific locations, using standard geophysical methods. Our findings underscore the potential of 3-D simulations to explore different scenarios, considering different survey configurations, source types and array sets.

Key words: Numerical modelling; Computational seismology; Earthquake ground motions; Surface waves and free oscillations; Waveform inversion; Wave propagation.

1 INTRODUCTION

The characterization of soil properties plays a significant role in numerous geotechnical and geophysical studies. In order to accurately characterize subsurface soil properties, various methodologies are utilized, including seismic reflection imaging, seismic refraction tomography, crosshole seismic tomography, downhole logging, surface wave analysis and full waveform inversion (FWI). Seismic reflection imaging involves analysing seismic reflection data to deduce the seismic velocities associated with distinct soil layers (Sheriff & Geldart 1995; Yilmaz 2001). Similarly, seismic refraction tomography uses seismic refraction data to delineate subsurface velocity profiles by analysing the traveltimes of seismic waves refracted at interfaces between geological layers (Telford *et al.* 1990; Mussett & Khan 2000). Crosshole seismic tomography allows the generation of detailed velocity distribution maps by acquiring seismic data from multiple boreholes at varying depths (Loke 2004). Downhole logging is another methodology that involves deploying geophysical instruments into boreholes to ascertain depth-specific velocity profiles. This technique offers insights into the vertical variation of soil properties and seismic velocities by measuring seismic wave velocities at discrete depths within boreholes (Telford *et al.* 1990). Surface wave analysis corresponds to a non-invasive

and cost-effective method of estimating shear wave velocities in the subsurface using the dispersive nature of surface waves (Park *et al.* 1999; Xia *et al.* 1999). Finally, FWI represents a sophisticated approach to generating high-resolution velocity models of the subsurface by leveraging the entire seismic waveform recorded at receivers. Unlike traditional methods that rely on simplified approximations, FWI iteratively refines velocity models to minimize the misfit between observed and simulated waveforms, yielding finely resolved images of subsurface structures. This technique finds applications in different scales (global, continental and regional) and fields such as oil exploration, earthquake imaging, and geothermal reservoir characterization (Tarantola 2005; Fichtner 2010).

Surface wave analysis is an effective technique for subsurface characterization, owing to its non-invasive nature, cost-effectiveness and capacity to offer complementary insights to other methodologies. Unlike drilling or extensive instrumentation, surface wave analysis utilizes seismic data acquired at or near the ground surface, minimizing the need for disruptive procedures and associated costs. Additionally, surface wave analysis takes advantage of the dispersive nature of surface waves, enabling the estimation of shear wave velocities across a range of frequencies. This frequency-dependent behaviour enables the characterization of shallow subsurface properties with high resolution, complementing the depth-focused ca-

pabilities of other techniques, such as seismic reflection imaging and downhole logging. Furthermore, the versatility of surface wave analysis in data acquisition and interpretation accommodates a variety of field conditions and geological settings. Due to its cost and time effectiveness, it has become a widespread technique for retrieving shear-wave velocity (V_s) profiles, contributing significantly to subsurface characterization. The basis of the surface wave analysis is to accurately determine the frequency-dependent phase velocity of fundamental-mode Rayleigh waves (Park *et al.* 1999), that is the experimental fundamental-mode dispersion curve. Different frequency components of surface waves travel at different velocities; this variation is known as the surface wave dispersion curve (O'Neill *et al.* 2003), and its computation requires processing the seismograms recorded on the field. Multiple methodologies have been developed to address this task, including the $p - \omega$ transform (McMechan & Yedlin 1981), the frequency-wave number ($f - k$) transform (Yilmaz 1987), the phase shift (Park *et al.* 1998), the wavelet transform (Kulesh *et al.* 2005; Holschneider *et al.* 2005) and the generalized S transform for phase velocity and group velocity. (Askari *et al.* 2011). Finally, the media's vertical V_s variation is estimated by solving an inverse problem based on the experimental dispersion curve (Foti *et al.* 2018).

In geotechnical engineering, surface-wave analysis dates back to the 1950s. The analysis utilizes input signals from either an artificial controlled source (active tests) or natural ambient vibration (passive tests). In the case of active source tests, the Spectral Analysis of Surface Waves (SASW) method, introduced by Nazarian & Stokoe (1984), marked a significant advancement in surface wave analysis. The SASW method improved testing with a two-receiver setup, which, combined with signal-analysis tools, allowed for measuring time delays between wave arrivals at the receivers. Initially, the method had limitations in terms of frequency band coverage. However, subsequent developments led to the creation of multistation approaches, which significantly improved efficiency and accuracy. The evolution continued with the introduction of multichannel analysis of surface waves (MASWs) by Park *et al.* (1999) in the late 1990s. Beyond active tests, passive methods emerged, leveraging microtremors generated by natural or human-induced activities. The passive approaches, including for instance the spatial autocorrelation (SPAC) method (Aki 1957, 1965) and refraction microtremor (ReMi) method (Louie 2001), enable the extraction of dispersion curves without active sources. In surface wave analysis, the first step is to obtain seismograms through either active or passive source surveys. The MASW is commonly used for active source surveys, while Passive Seismic Ambient Noise Correlation (SPAC) is popular for passive source surveys. However, the choice of method depends on specific research objectives, geological conditions and available resources. The second stage of surface wave analysis involves seismogram processing, which includes calculating the dispersion curve based on experimental data using for instance the frequency-wave number ($f - k$) method. Finally, the dispersion curve inversion involves determining the V_s profile by optimizing model parameters. This optimization implies minimizing the differences between the experimental dispersion curve (target) and a large set of computed dispersion curves estimated based on soil profiles characterized by the combination of user-defined soil parameters.

Different projects have been implemented to improve the application of surface-wave methods (Cornou *et al.* 2006; Bard *et al.* 2010; Tran & Hiltunen 2011; Cox *et al.* 2014; Asten *et al.* 2014). In response to the lack of standardization in the practice and interpretation of surface wave methodologies, the InterPACIFIC project was carried out (Garofalo *et al.* 2016a, b). Its goal was to compare

the most common techniques for surface wave analysis to assess their reliability and performance. The study examined surface-wave propagation across three sites with varying subsoil conditions. Different teams analysed the same raw data independently. Despite varying strategies, the estimated dispersion curves showed good agreement, indicating robust processing procedures. However, some subsoil features remained unclear, leading to variations in results, especially in identifying interface positions. The study emphasized the importance of incorporating *a priori* information, such as local geology and borehole logs, to enhance reliability and highlighted the impact of solution non-uniqueness on uncertainties. Furthermore, the use of additional data analysis techniques, such as critically refracted P waves and Rayleigh ellipticity, to improve bedrock identification and parameter estimation was suggested. Although variability was observed, it was more limited in estimating average parameters like V_{S30} , compared to individual layer thickness.

3-D physics-based simulations can help understand the sources of variability observed in surface wave analysis. The increasing use of these simulations is due to advancements in high-performance computing (HPC) and applications, especially in areas where detailed models of the structure of crustal and sedimentary basins are available. However, it is essential to note that these simulations are sensitive to parameters like the velocity model, attenuation parameters and source characteristics. Among these parameters, the seismic-velocity model is critical to achieving a high-quality match between simulated and observed data (Taborda & Roten 2015). This study explores the potential use of physics-based simulations as a virtual test laboratory to replicate *in situ* tests for surface wave analysis. The study focuses on an array configuration for active and passive sources within the Argostoli Basin, Greece. Initially, we used a laterally homogeneous velocity model with basin geometry-induced heterogeneity (Cushing *et al.* 2020). However, future efforts will introduce medium variability by incorporating random spatially correlated perturbations into the velocity model. The velocity model available for the Argostoli Basin was validated, followed by 3-D simulations of virtual *in situ* tests of active and passive sources. The simulations were conducted using SEM3D (CEA, CentraleSupélec, IPGP, and CNRS 2017; Touhami *et al.* 2022), a 3-D spectral element simulator, utilizing HPC resources. The synthetic seismograms were processed in GEOPSY (Wathelet *et al.* 2020), a software package commonly used in academic research and industrial applications for various purposes, such as processing seismic data, calculating dispersion curves, and conducting surface-wave inversion. The subsequent sections elaborate on the study site, methodology and outcomes.

2 REALISTIC CASE STUDY: ARGOSTOLI BASIN

The availability of the geological structure and *in situ* test results make this region a compelling study case. The basin is predominantly comprised of Lagoonal Quaternary sediments, which overlay the infill of an active Plio-Quaternary syncline. Additionally, the region exhibits pronounced tectonic activity, marked by substantial folding and faulting of the Plio-Quaternary series, as documented by Cushing *et al.* (2020). We simulated active and passive source tests (MASW and SPAC, respectively) and compared our results to data available at the ARGONET borehole. Simulation results were analysed in the vicinity of this location (following different arrays configurations) to obtain the material properties from the inversion of the synthetics. The 3-D simulations were conducted in

Table 1. Location in the UTM Z34N coordinate system and dimensions of the simulation domain.

| Direction | Coordinates [m] | Dimension [m] |
|-----------|------------------------|---------------|
| EW | 452 850 to 461 325 | 8475 |
| NS | 4 219 800 to 4 228 280 | 8475 |
| UD | −2980 to 0 (depth) | 2980 |

SEM3D, considering linear-elastic behaviour. The material quality factors were assigned based on values used in simulations previously conducted for this same region (Touhami 2019). The mesh was generated following the not-honouring approach (mesh does not follow the domain geometry), and the minimum element size was set as $5 \text{ m} \times 5 \text{ m} \times 5 \text{ m}$ to attain the resolution needed in terms of frequency ($f_{\text{max}} = 30 \text{ Hz}$). The vertices coordinates and dimensions of the region of study are listed in Table 1. In this table, horizontal coordinates are presented in the Universal Transverse Mercator (UTM) coordinate system for the zone 34 north (Z34N). Domain dimensions are presented in metres.

The material properties (V_p , V_s , ρ) were obtained from the model developed by Cushing *et al.* (2020). In their study, the authors identify three material categories (soft soils, stiff soils, and rock material) and provide a set of equations for each category that characterizes the shear wave velocity variation between geological boundaries. These geological boundaries are available in rasters that define the limiting depth of the corresponding geological structure. Fig. 1 shows the variation of the material properties at the simulation domain's surface. On the surface, and based on the equations, it can be observed that the minimum shear wave velocity value is 250 m s^{-1} . However, this value decreases as depth increases, reaching a minimum of approximately 168 m s^{-1} at a depth of 5 m in the simulation due to the simulation's resolution, with a minimum element size of 5 m. Previous field studies have documented the minimum value at a depth of 2 m, which is attributed to the presence of artificial deposits in the form of man-made infill atop the underlying alluvial deposits (Hollender *et al.* 2018; Cushing *et al.* 2020). The spatial variation of the velocity model is considered using a 3-D mesh that captures the changes in velocity properties and geometry of the basin. Fig. 2 presents a visual representation of the (a) basins' bottom and (b) the mesh to highlight the tridimensionality of the model when considering the geometrical variation of the basin's shape. The two interfaces depicted in Fig. 2(a) illustrate the basin's material composition, distinguishing between soft and stiff materials as defined by Cushing *et al.* (2020). According to the authors, coordinates falling within the green volume are assigned to soft soil. Similarly, coordinates situated deeper than the soft soil layer and extending to the pink interface are classified as stiff soil. Any material outside these two delineated interfaces is attributed to rock composition. Furthermore, Fig. 3 presents the shear wave velocity variation in the proximity of the ARGONET borehole coordinates. This figure illustrates the geometric changes in the basin's shape with depth in the profiles A–A' and B–B'. As depicted, the basin's deepest portion is situated to the west of the ARGONET borehole. The plan location of cross-sections A–A' and B–B' is detailed in Fig. 2.

3 VALIDATION OF THE ARGOSTOLI BASIN SIMULATION

ARGONET consists of Kinometrics accelerometers, one vertical array disposed on the basin (soil site) with one station at the surface and four down-hole stations located at the bottom of four different

boreholes, at 5.6, 15.5, 40.1 and 83.4 m depth (Theodoulidis *et al.* 2018). In their study, Hollender *et al.* (2018) identifies these stations as AS0, AS6, AS15, AS40 and AS83. We keep those names to establish the comparison between both studies. In addition, ARGONET also has an outcrop station (at rock on the surface, called AR0) that we did not include in the present study; however, it can be considered in future computations. Hollender *et al.* (2018) calculated the spectral soil ratio (SSR) at the site using 436 recorded earthquakes with magnitudes ranging from M_1 1.6 to M_w 6.4, and with epicentral distances varying from 1 to 200 km, which corresponds to the data set retrieved at ARGONET in the period from July 2014 to April 2017. In their study, the authors present the results of the large set of SSRs using geometric means and geometric standard deviations. The SSRs were calculated as the spectral ratio between the data at AS0, AS6, A15 and A40 with respect to the data gathered at the borehole station at the bedrock level AS83.

To validate our simulations, we calculated spectral ratios at various depths (AS0, AS15 and AS40) with reference to AS84, where 84 m represents the depth at which the bedrock station was simulated. These results were then compared to findings previously published by Hollender *et al.* (2018). To achieve this, we generated two incident ground motions using different methodologies: one based on plane wave propagation (PW) and the other utilizing a double-couple point source (PS). For the plane wave propagation, we constructed a model using a grid of point sources laid out over a mesh spanning dimensions of 14 180 m by 14 180 m, arranged in a horizontal plane. These sources were spaced based on the Gauss–Lobatto–Legendre (GLL) points' positions at 20 000 m depth. The point source was configured as a double-couple source, following an approach similar to that detailed by Touhami (2019). The temporal evolution of the displacement adhered to the source model proposed by Brune (1970) and the point source parameters were characterized based on prior work by Gatti (2017). The seismic event's magnitude was specified as M_w 4.6 with strike = 163° , dip = 39° and slip = 92° . The source's UTM Z34N coordinates (x , y) were (2 275 400 m, 4 242 100 m) at 14 000 m. Both simulations shared identical mesh and material properties, differing primarily in the source definition. Table 2 provides an overview of the computational resources used and key parameters common to both simulations. Additionally, Fig. 4 presents synthetic ground motion data for the PW source propagation at ARGONET, showcasing results at four distinct depths: surface (darker blue line), 15 m (lighter blue line), 40 m (yellow line) and 84 m (red line), for all three motion components (EW, NS and UD).

Synthetics presented in Fig. 4 were used for computing the site response. These results were compared to data registered on the field and are shown in Figs 5 and 6. In Fig. 5, the continuous red line shows the SSR calculated as the ratio between AS0/AS84 for the results of the PW simulation. The red dashed line represents the same calculation for the PS simulation. In addition, the black lines depict the results by Hollender *et al.* (2018). The continuous black line represents the geometric mean, and the dashed black lines represent the geometric standard deviations. As shown in the figure, there is a good agreement in the shape of the spectral soil ratios, the natural frequency and its amplitude when compared with simulated data for both cases: plane wave propagation and point source. Fig. 6 shows the SSR computed at different depths in the ARGONET vertical array using the bedrock sensor as reference (AS83 in Hollender *et al.* 2018, and AS84 in this study). The colored lines represent the simulation results (continuous lines for PW and dashed lines for PS). In addition, the black lines depict Hollender *et al.* (2018) geometric mean results at different depths.

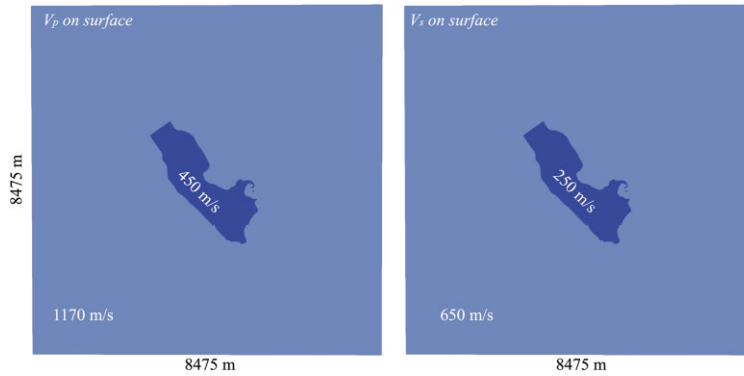


Figure 1. Spatial variation on surface of the P -wave and S -wave velocities in the Argostoli region.

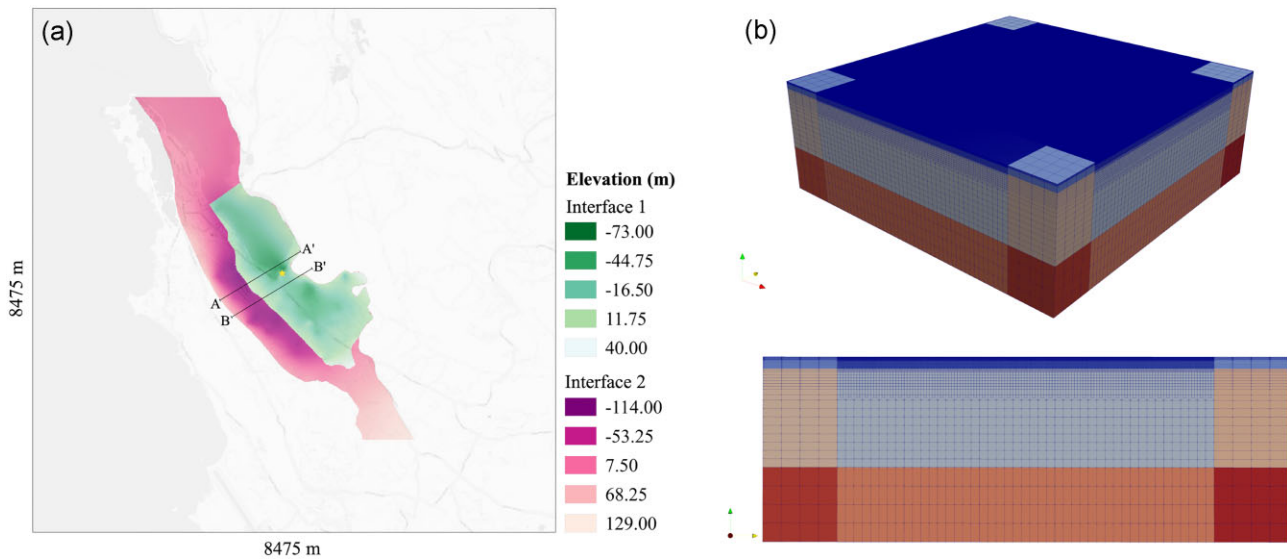


Figure 2. (a) Interfaces defining basin's bottom for soft and stiff soils as described by Cushing *et al.* (2020) and (b) mesh used in SEM3D to simulate the active and passive source tests (MASW and ambient noise).

Similar to the findings illustrated in Fig. 5, the comparison between field measurements and simulations demonstrates a favourable alignment in terms of natural frequency and site response amplitude. While slight disparities become noticeable at higher frequencies, Figs 5 and 6 showcase a strong concordance in both the shape and magnitude of site responses between the simulated and experimental data sets. The discrepancies observed at higher frequencies are mainly due to the lateral homogeneity of the velocity model. The results obtained in Hollender *et al.* (2018) were derived from various techniques such as cross-hole, down-hole, surface-wave-based methods and seismic interferometry at the actual site. This approach encapsulated the natural variations of soil in the vicinity of ARGONET. However, the velocity model used in our simulations simplified the properties of the region by assuming it to be laterally homogeneous. As a result, our simulations could not capture the contribution of the inherent soil heterogeneities to the higher frequency content of ground motion. Furthermore, prior investigation by Imtiaz *et al.* (2021) delves into the impact of edge-diffracted surface waves on the site response within the basin, particularly at higher frequencies. It's possible that in our scenario, the nature of the seismic source utilized might impose limitations

on the generation of such surface waves, influencing the observed differences.

4 SIMULATION OF ACTIVE SOURCE TESTS

4.1 Initial condition for the inversion

We used DINVER, which is a component of the Geopsy software suite. Geopsy is a commonly used set of geophysical software tools tailored for geophysical inversion and modelling, as described by Wathelet *et al.* (2020). The initial condition for the inversion was defined based on data available from previous studies. Fig. 7 shows the properties at the ARGONET borehole site. Three geotechnical layers were obtained from the study by Hollender *et al.* (2018). The authors identify artificial deposits, clays and sandy marls and gravels with corresponding thicknesses of approximately 2, 8 and 69 m. These geotechnical layers depths are showed in Fig. 7. The green line depicts the shear wave variation in depth extracted from the SEM3D mesh. The black line corresponds to the material properties at the ARGONET borehole site calculated with the set of

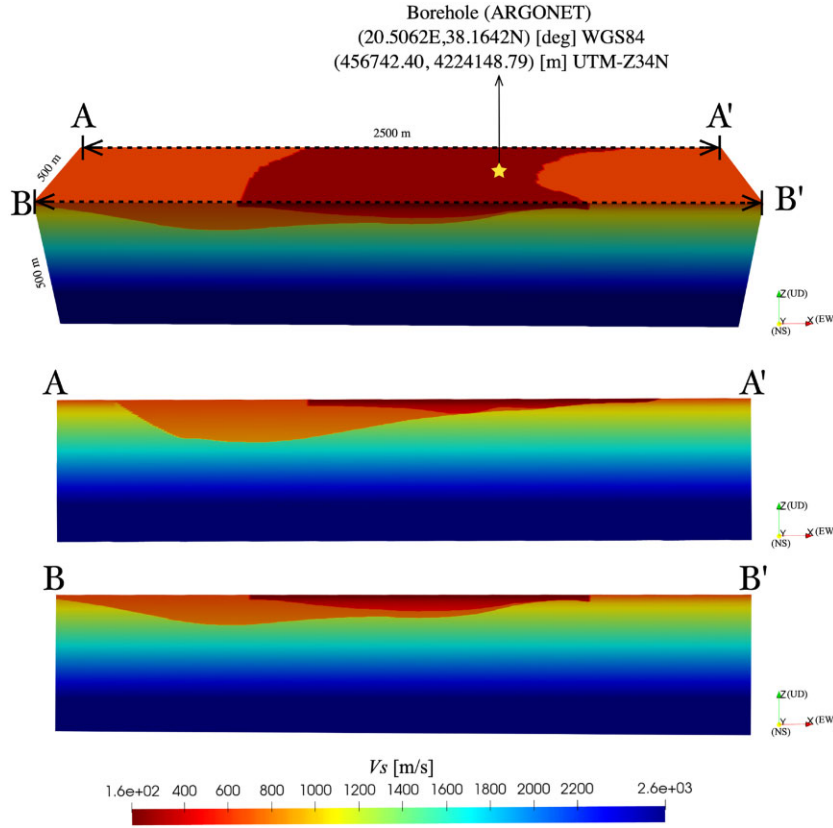


Figure 3. Shear-wave velocity variation on depth near the borehole location.

Table 2. Summary of some of the parameters and computational resources used for the plane wave and point source simulations.

| Parameter | PW |
|--|---|
| Number of processors | 720 |
| Wave max. freq [Hz] | 10 |
| Min. V_s [m s^{-1}] | 250 |
| Simulation time [s] | 30 |
| Delta time [s] | 0.000253 |
| Total number of elements [m] | 15 575 393 |
| Dimension [$\text{m} \times \text{m} \times \text{m}$] | $24\,675 \times 24\,675 \times 61\,200$ |
| Total wall clock [hh:mm:ss] | 20:00:00 |
| Running time/simulation time | 2400 |

equations by Cushing *et al.* (2020). The differences between the black and green line are due to the mesh's resolution (min. element size in depth equal to 5 m) and the interpolation between GLLs. Nonetheless, it can be observed that the values of both material models are close in depth. The red and pink discontinuous lines correspond to two additional models available in Hollender *et al.* (2018) at this same site. Based on the data available from the material structure (V_p , V_s , ρ), 15 sets of initial conditions were defined as input for the inversion. These sets correspond to a combination of an initial number of layers (thicknesses), average V_s profile and range of variation of the average V_s profile, which was used to define the V_p and V_s limits. The procedure followed to define the input parameters for the inversion is presented below. In addition, Table 3 summarizes the properties used for each inversion case.

(i) Initially, a number of layers was assumed to discretize the profile showed in Fig. 7. For instance, in Table 7 cases 1–3 were

discretized with nine layers and with a wider thickness range for the inversion compared to cases 4–6. These cases were defined to understand the inversion results dependence on the parametrization. In this study, narrow or wide search properties that may or not be based on existing geotechnical information define the input parameters.

(ii) The layered representation of the soil profile (blue dotted line in Fig. 7) was calculated using eq. (1).

$$\bar{V}_s(h) = \sum H_i / \sum H_i / V_{si} \quad (1)$$

where H_i are the thicknesses of the i th subpartitions of the initial N layers (e.g. 9 in cases 1–6) in a certain number of sublayers (e.g. 100 subpartitions per initial layer).

(iii) The input V_s ranges for the inversion (blue area in Fig. 7) are defined as $\pm P$ of the average profile calculated above. In this study, P was evaluated as 5, 10 and 20 per cent. V_p was computed as 1.8 times the value of V_s and the density is defined as 2400 kg m^{-3} based on the material model data.

The ranges of V_s (5, 10 and 20 per cent) do not represent the aleatory variability of soil properties. Instead, these percentages set constraints for the inversion problem by specifying minimum and maximum values for V_s , V_p and ρ within each layer. In practical field applications, such limits would be determined from collected data. It is important to note that the velocity model used in this work is laterally homogeneous. This means that any spatial variability within the velocity model was not taken into account in the simulations, except for the heterogeneity induced by the basin's shape. To account for the spatial variation of the material, two methodologies could be followed when using physics-based simulations. The first method involves using a 3-D model, which includes the variability

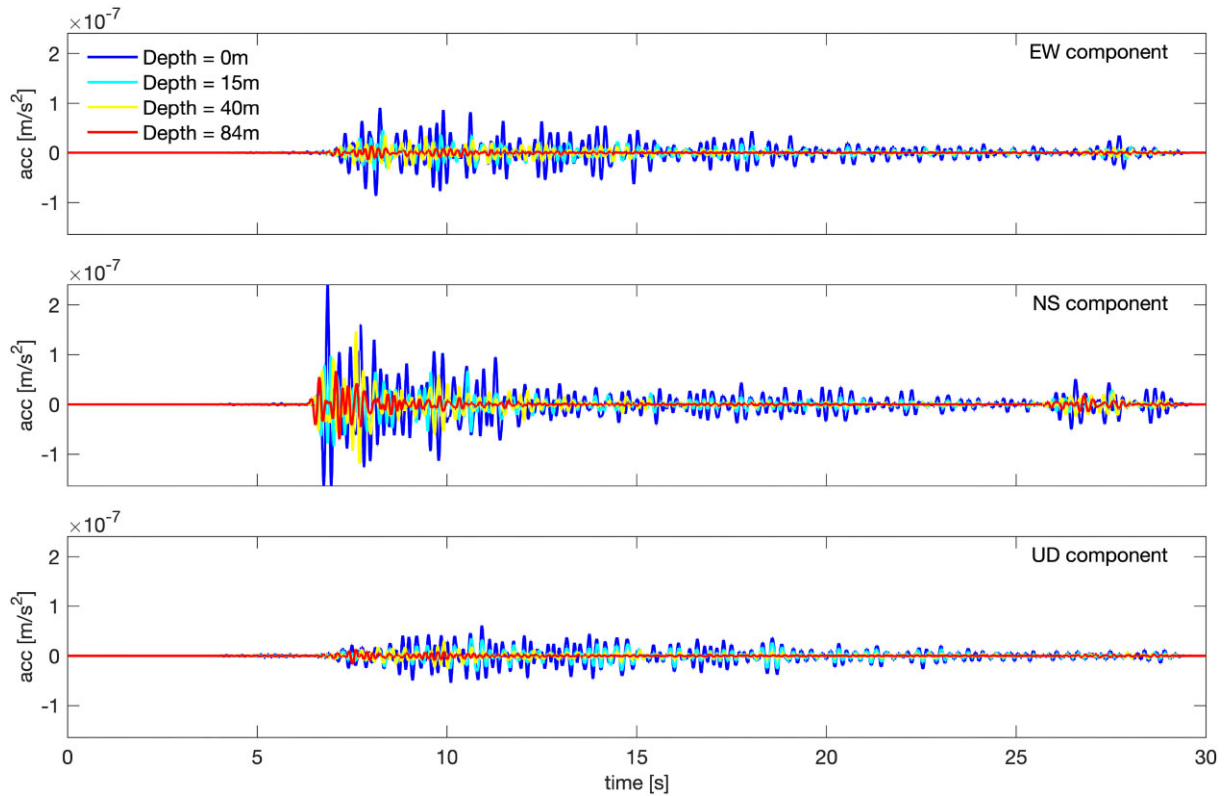


Figure 4. Acceleration time-series at the ARGONET station obtained in the PW simulation (bandpass filtered 0.15–10 Hz).

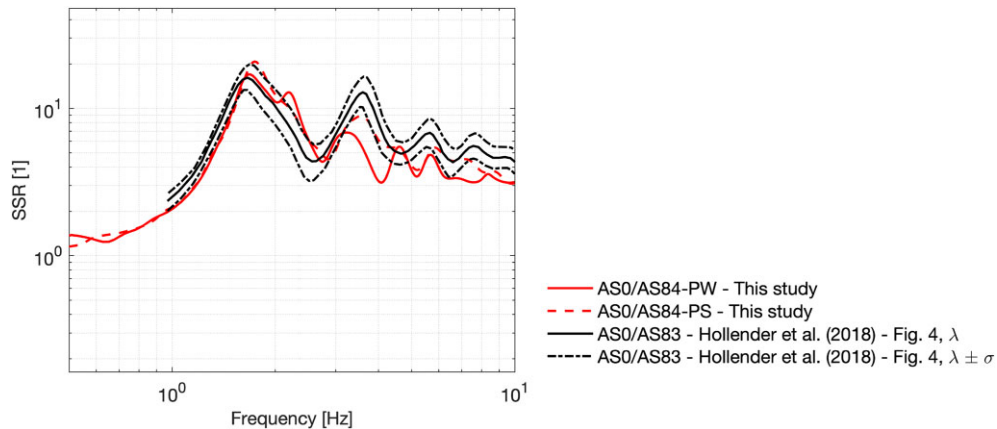


Figure 5. Comparison of the spectral soil ratios between receivers at surface and the borehole at 84 m depth. Red lines represent results for the simulation (continuous line for PW and dashed lines for PS). Black lines correspond to experimental data at the same site (ARGONET) published by Hollender *et al.* (2018).

of the material, and then conducting the simulation of the *in situ* test and a normal inversion process (which follows a 1-D layered soil hypothesis). This approach allows testing the hypothesis of the 1-D model commonly used in the practice. As previously mentioned, the velocity model is laterally homogeneous. The variability of the soil properties will be considered as part of future activities to be developed within the project's scope. This can be done in SEM3D by using one of the software's branches that allow including variability coefficients to account for the spatial variability of soil properties. The second method involves conducting a 2-D or 3-D inversion that considers the spatial variability in the material model, via FWI.

4.2 Linear array configuration

The acquisition layout is presented in Fig. 8. The blue star represents the active source location. Red triangles depict the localization and configuration of the 'geophones' array used to conduct f - k analysis of the active source.

The selection of the array was based in the article by Foti *et al.* (2018) 'Guidelines for the good practice of surface wave analysis: a product of the InterPACIFIC project'. The array's size and the spacing between geophones determine the wavelengths range over which the dispersion curve can be obtained. The theoretical limits associated with the array were calculated using the expressions

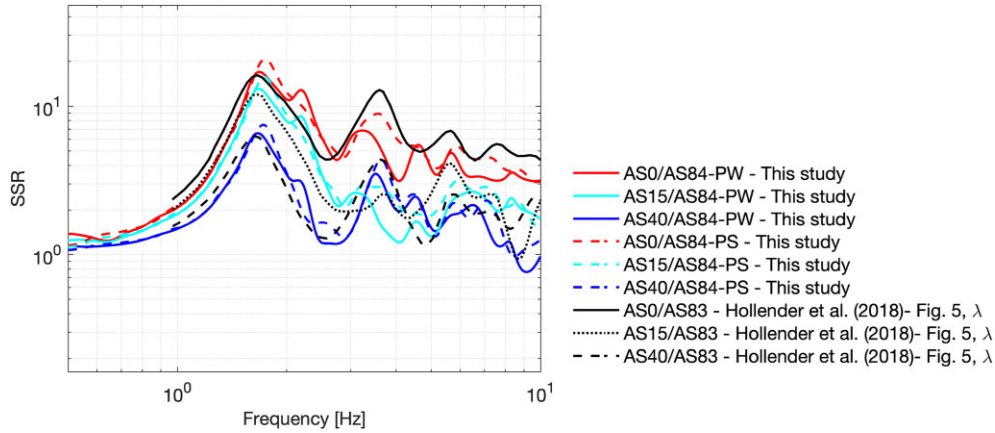


Figure 6. Comparison of the spectral soil ratios between receivers at surface, 15 m depth and 40 m depth with respect to the borehole at 84 m depth. Colored lines represent results for the simulation (continuous line for PW and dashed lines for PS). Black lines corresponds to experimental data at the same site (ARGONET) published by Hollender *et al.* (2018).

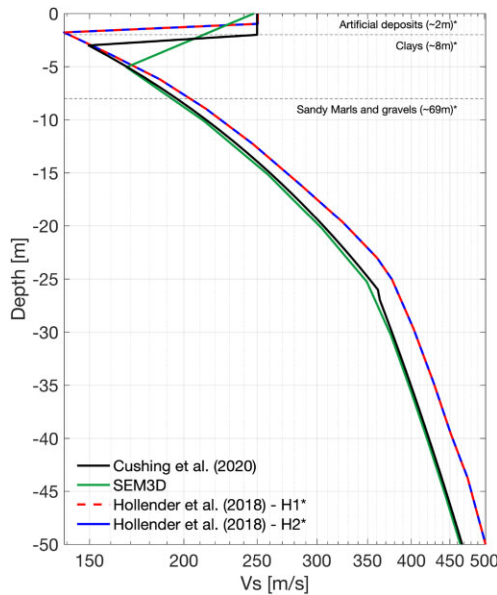


Figure 7. Material models available in the literature, model extracted from the mesh used in SEM3D at the ARGONET borehole site, and characterization of a layered model to define the initial conditions for the inversion.

presented below for linear arrays as recommended in Foti *et al.* (2018).

$$\lambda_{\min} \sim 2\delta_x \quad (2)$$

$$\lambda_{\max} \sim L \quad (3)$$

where λ_{\min} and λ_{\max} are the minimum and maximum wavelengths, respectively. δ_x is the linear array spacing and L is the length of the linear array. The theoretical limits for the array used in the study is listed in Table 4. The minimum near-surface layer thickness resolved and expected maximum investigation depth were also evaluated as recommended by Foti *et al.* (2018), and can be approximated as shown below.

$$h_{\min} \sim \lambda_{\min}/3 \text{ to } \lambda_{\min}/2 \quad (4)$$

$$h_{\max} \sim \lambda_{\max}/3 \text{ to } \lambda_{\max}/2 \quad (5)$$

4.3 Simulation parameters








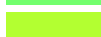







Simulation parameters are listed in Table 5. The source was characterized by a vertical force applied at the surface and situated at the ARGONET borehole coordinates. Furthermore, the input source function was derived from a falling weight deflectometer (FWD) test, with the temporal variation of the force illustrated in Fig. 9.

4.4 Results

In the current study, the inversion process was carried out using DINVER. The user is required to input possible limit values for the various parameters, such as layer thickness, P and S -wave velocity ranges and density values. The software uses a Montecarlo approach to generate multiple soil profiles and their corresponding dispersion curves, which are then compared to the recorded data's dispersion curve using a shape misfit. It is important to note that, in practice, the dispersion curve of a site of interest is unknown. Therefore, the inversion process is performed to obtain it. One notable aspect of this study is the use of prior knowledge regarding the site's material properties to construct the 'real' material dispersion curve, thereby establishing a reference point for comparison (reference curve).

Fig. 10(a) shows a comparison of the 100 best stratigraphy models generated by DINVER for each inversion scenario. The solid black line represents the actual velocity model derived from SEM3D data. We further analysed a subset of the top 10 models from each inversion to assess their fit to dispersion curves and site response characteristics. The best dispersion curves are illustrated in Fig. 10(b). The solid black line represents the target dispersion curve obtained from synthetic data. In contrast, the dashed black line shows the reference dispersion curve derived from the actual velocity model using GPlivemodel. GPlivemodel is a tool in GEOPSY that computes Rayleigh waves' fundamental mode based on a 1-D soil column description. The dashed black lines denote the array's wavelength limits, following Foti *et al.* (2018). Additionally, the blue dashed line indicates the maximum wavelength limit ($0.4 \times L$) according to the criterion proposed by O'Neill *et al.* (2003). The results demonstrate a strong agreement between the inverted profiles and the theoretical curve, particularly up to a minimum wavelength of $0.4 \times L$, supporting the conservative criterion by O'Neill *et al.* (2003) Finally, we selected a final set of 25 stratigraphy profiles to conduct 1-D analyses. The selection was based on their fit to the

Table 3. Summary of the input parameters per inversion case. The color code is related to results presented in Figs 10–14. Each color represents an inversion case in the result figures presented in the following section.

| Color | Case | N layers | Max. layer thickness [m] | V_s range | Criteria |
|---|------|----------|-----------------------------|-------------|-----------------------|
|  | 1 | 9 | [5 10 10 10 10 10 10 10 10] | 20 per cent | Geotechnical layers |
|  | 2 | 9 | [2 6 7 5 5 5 5 5 5] | 20 per cent | Geotechnical layers |
|  | 3 | 9 | [5 10 10 10 10 10 10 10 10] | 10 per cent | Geotechnical layers |
|  | 4 | 9 | [2 6 7 5 5 5 5 5 5] | 10 per cent | Geotechnical layers |
|  | 5 | 9 | [5 10 10 10 10 10 10 10 10] | 5 per cent | Geotechnical layers |
|  | 6 | 9 | [2 6 7 5 5 5 5 5 5] | 5 per cent | Geotechnical layers |
|  | 7 | 5 | 10 for all layers | 20 per cent | Naive parametrization |
|  | 8 | 10 | 5 for all layers | 20 per cent | Naive parametrization |
|  | 9 | 25 | 2 for all layers | 20 per cent | Naive parametrization |
|  | 10 | 5 | 10 for all layers | 10 per cent | Naive parametrization |
|  | 11 | 10 | 5 for all layers | 10 per cent | Naive parametrization |
|  | 12 | 25 | 2 for all layers | 10 per cent | Naive parametrization |
|  | 13 | 5 | 10 for all layers | 5 per cent | Naive parametrization |
|  | 14 | 10 | 5 for all layers | 5 per cent | Naive parametrization |
|  | 15 | 25 | 2 for all layers | 5 per cent | Naive parametrization |

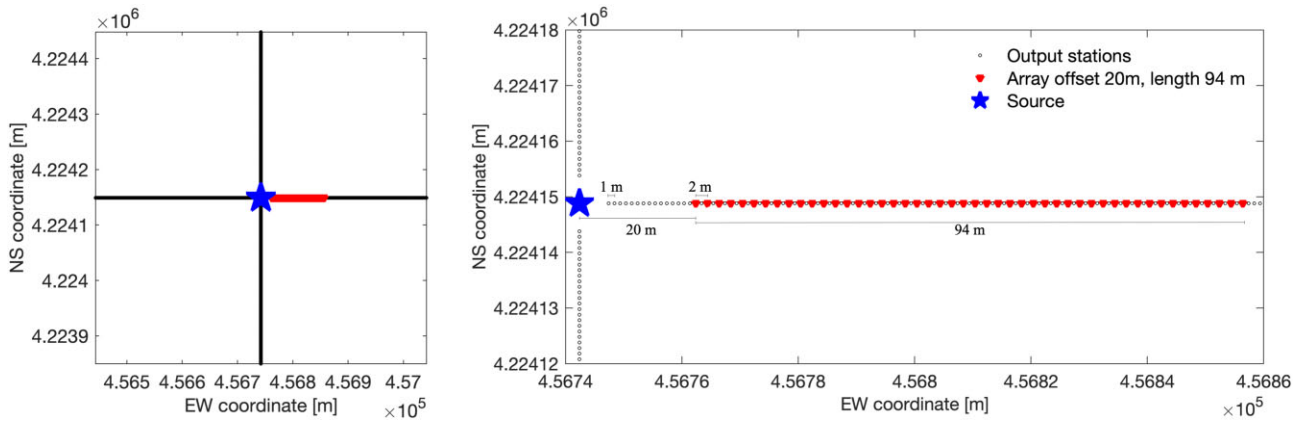


Figure 8. Output stations location and the array configuration used in the MASW analysis.

Table 4. Theoretical wavelength limits.

| Array | Simulation | Offset [m] | δ_x [m] | L [m] | λ_{\min} [m] | λ_{\max} [m] | h_{\min} [m] | h_{\max} [m] |
|-------|------------|------------|----------------|---------|----------------------|----------------------|----------------|----------------|
| 1 | ARGO MASW | 20 | 2 | 94 | 4 | 94 | [1.3, 2] | [31.33, 47] |

Table 5. Summary of the MASW simulation parameters and computational resources used.

| Parameter | MASW |
|----------------------------------|--------------------------------|
| Number of processors | 2000 |
| Wave max. freq [Hz] | 30 |
| Min. V_s [m s^{-1}] | 168 |
| Simulation time [s] | 4 |
| Delta time [s] | 0.000121 |
| Min. element size [m] | 5 |
| Dimension [m] | $8475 \times 8475 \times 2980$ |
| Total wall clock [hh:mm:ss] | 12:00:00 |
| Running time/simulation time | 21 600 |

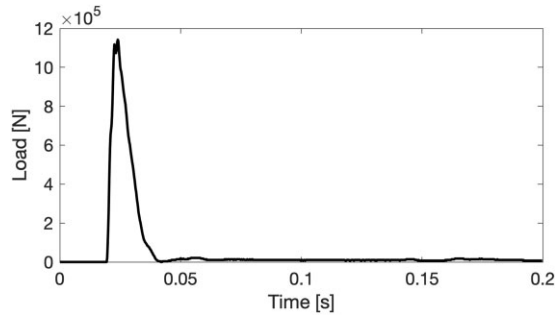


Figure 9. Vertical force in time applied at the ARGONET borehole coordinates to simulate the active source.

target dispersion curve among the 150 best profiles identified. The goodness of fit was based on the misfit between the target dispersion curve and the 150 curves computed in GPlivemodel, calculated using the expression proposed by Wathelet *et al.* (2004), which aligns with the approach used in DINVER (see eq. 6). The summary of the minimum, maximum and median values of the misfit is presented in Table 6

$$misfit = \sqrt{\sum_{i=1}^{n_f} \frac{(x_{di} - x_{ci})^2}{\sigma_i^2 n_f}} \quad (6)$$

where x_{di} is the velocity of the data curve at frequency f_i , x_{ci} is the velocity of the calculated curve at frequency f_i , σ_i is the uncertainty of the frequency samples considered. If no uncertainty is provided, σ_i is replaced by x_{di} and n_f is the number of frequency samples considered.

Illustrated in Fig. 11 are the dispersion curves for four inversion cases: Case 1, 6, 9 and 13. This comparison allows for an analysis of how the variation in criteria for selecting inversion parameters affects the overall results. In all subplots of the figure, the black dashed line represents the target dispersion curve, which is obtained from SEM3D synthetics. The star markers depict the dispersion curve of the ‘real’ material model (reference curve). The colored continuous lines show the median of the 10 best dispersion curves for each case, and box plots are used to display the 25th, 50th and 75th percentiles at each frequency. Case 1 considers geotechnical layer parameters in its parametrization, which is also the criteria used in cases 1–6. Cases 9 and 13 represent results for input layers and thicknesses that do not follow specific criteria in their selection, referred to as ‘naive’ parametrization. In practice, soil properties are often obtained through blind prediction, but in our study, we have prior knowledge of the ‘real’ soil properties. The reference dispersion curve, which is based on known properties, differs from the target dispersion curve obtained from synthetics. Notably, both curves exhibit similar behaviour for frequencies greater than 6 Hz, while differences become more pronounced at lower frequencies. This observation may be related to the resolution of the MASW test and the type of loading. The resolution of the active source test tends to improve at higher frequencies, primarily because resolution at shallow depths is influenced by high-frequency data (shorter wavelengths). Furthermore, our simulations suggest that the proposed value of $L_{max} = L$ following Foti *et al.* (2018) is relatively high. In contrast, O’Neill *et al.* (2003) limit provides a more suitable threshold for establishing the validity of the dispersion curve.

When examining the various inversion cases depicted in Fig. 11, it is observed that results tend to improve when the input parameters, including layer thicknesses and velocities, cover a wider range and comply with geotechnical criteria. For instance, comparing the inversion results of Case 1 and Case 6 highlights this improvement.

In scenarios where input parameter ranges become narrower, differences between the dispersion and target curves tend to grow. In such cases, the dispersion curves obtained from the inversion process closely resemble a single profile defined by the limited input search range. It is worth noting that the user’s criteria when formulating the inversion process can introduce biases into the results. Furthermore, we draw attention to the influence of the maximum wavelength limit. At frequencies below 6 Hz, we observe an increasing discrepancy between the soil profiles derived from inversion and their corresponding dispersion curves, in contrast to the soil profile and reference curve known *a priori*. Based on the results obtained, we have found that adopting the more conservative wavelength limit proposed by O’Neill *et al.* (2003) closely matches the soil profiles and dispersion curves with the desired properties. Utilizing this criterion constrains the exploration depth to 13–19 m. Our study shows optimal inversion results within this depth range. However, it is important to acknowledge that this observation is contingent upon the specific conditions of the simulations.

After comparing the inversion results to the reference curve, it becomes apparent that the ‘naive’ parametrization yields results closer to the reference curve in certain cases (e.g. case 9). Additionally, there is greater variability in the shape of the median dispersion curve among inversion cases following the ‘naive’ parametrization (e.g. compare cases 9–15). Conversely, basing the parametrization on geotechnical criteria leads to a better match with the reference curve at low frequencies but increasing differences at high frequencies. Furthermore, adhering to this criterion reduces the variations in the shape of the median curves among the inversion cases (e.g. compare cases 1–6). Obtaining dispersion curves closely resembling the ‘real’ material (reference) curve through a ‘naive’ parametrization may seem contradictory. However, we used numerous layers with narrow input parameter ranges, causing the code to generate results constrained by the user-defined input parameters. In practical field tests, the objective is to find soil profiles whose dispersion curves are similar to those derived from field data (the ‘target’ curve). The ‘reference’ curve is unknown and calculated from field data in real-world scenarios. Therefore, the ‘reference’ curve aligns with the ‘target’ curve. Nevertheless, due to the nature of our study, we already know the ‘reference’ curve, allowing us to make interesting observations.

Even though using many layers with low thickness (e.g. 2 m) results in soil profiles closely resembling the ‘real’ material, using such criteria is impractical. The level of resolution required for input data to define these inversion parameters would imply that the actual properties of the site are known, eliminating the need for field testing or blind predictions. Alternatively, the narrow input inversion parameters introduced a bias in the response. As seen in cases 7–15, the resulting dispersion curves do not exhibit a similar shape to those obtained from field data (synthetics in this study), as the actual material is unknown (blind prediction). Additionally, it is important to consider that the minimum wavelength is related to the lowest exploration thickness of the array Foti *et al.* (2018). Our findings are consistent with conclusions drawn in previous studies, supporting the effectiveness of active source tests such as MASW for high frequencies, while also indicating limitations in capturing low-frequency information. In such situations, a combined approach incorporating passive source testing and exploring various array configurations to improve depth resolution is advisable.

The best 25 stratigraphy models obtained are shown in Fig. 12. As shown in this figure, different models provide similar goodness of fit with the recorded data (SEM3D synthetics). As previously

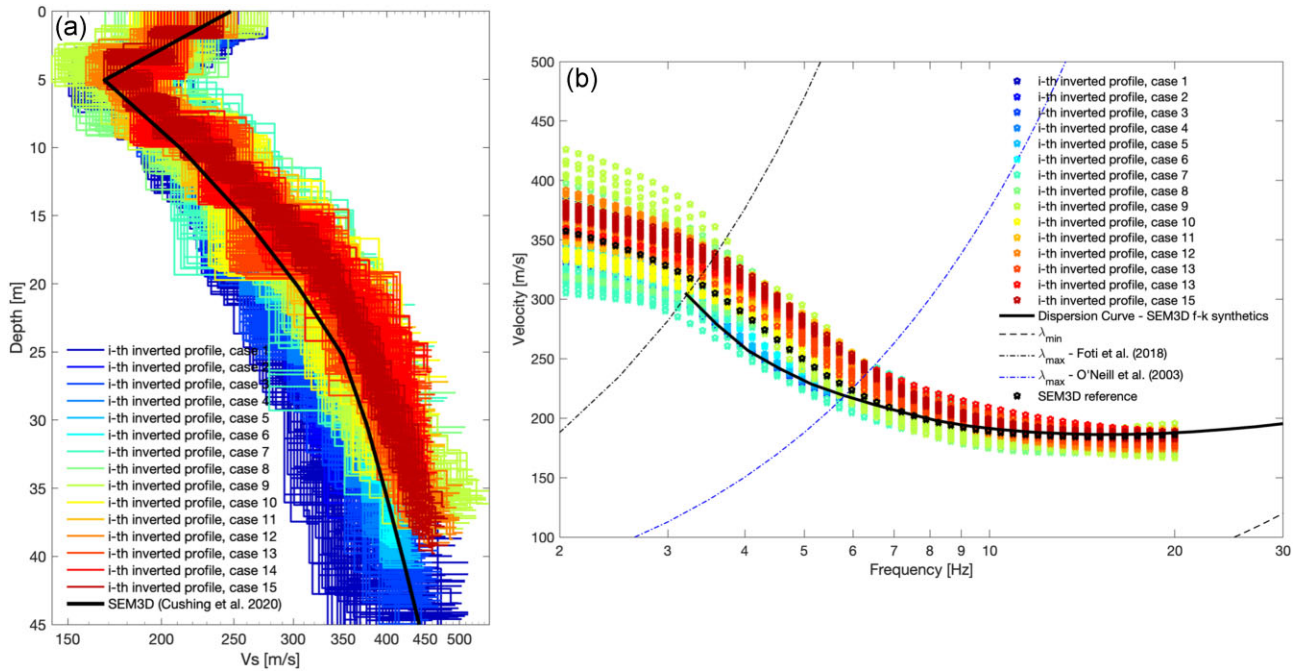


Figure 10. V_s profiles obtained from inversion. The figure shows the 100 best profiles per inversion case based on the misfit calculated by DINVER. Dispersion curves for the 10 V_s profiles with lowest misfit per inversion case. The wave length limits corresponding to the array configuration are shown.

Table 6. Summary of misfit values for each inversion case.

| Inversion case | Min(misfit) | Max(misfit) | Median(misfit) |
|----------------|-------------|-------------|----------------|
| 1 | 2.7426e-05 | 0.00011685 | 4.9294e-05 |
| 2 | 5.2164e-05 | 0.00010067 | 8.544e-05 |
| 3 | 3.9096e-05 | 0.00011725 | 8.2364e-05 |
| 4 | 7.7436e-05 | 0.00011224 | 9.5557e-05 |
| 5 | 0.00010398 | 0.00011592 | 0.00011253 |
| 6 | 0.00035245 | 0.00047735 | 0.00042754 |
| 7 | 0.0026773 | 0.0086854 | 0.0054078 |
| 8 | 0.003832 | 0.01225 | 0.0058201 |
| 9 | 0.003832 | 0.01225 | 0.0071757 |
| 10 | 0.0036157 | 0.010513 | 0.0059246 |
| 11 | 0.0057992 | 0.012421 | 0.010484 |
| 12 | 0.0078841 | 0.012425 | 0.010423 |
| 13 | 0.0062436 | 0.011903 | 0.0076399 |
| 14 | 0.011903 | 0.011903 | 0.011903 |
| 15 | 0.010183 | 0.012391 | 0.011571 |

discussed, narrow inversion ranges can produce significant differences in the dispersion curve shape. Even though misfit values can be low in all cases, better results in terms of the shape of the dispersion curve may be obtained when considering wider ranges for the wave velocities and definition of the number of layers and thicknesses based on available geophysical data (cases 1–6) and not by following a ‘naive’ parametrization (as in cases 7–15). In addition, we analysed the seismic response of the 1-D models previously obtained. We modelled the inverted soil profiles in the software DEEPSOIL (Hashash *et al.* 2016) and calculated the soil spectral ratio (SSR) between the surface response and the one corresponding to the borehole at 40 m depth. The SSR is calculated as the square root of the ratio of the geometric mean of the horizontal components of motion between the Fourier spectrum at the surface and borehole level, as shown in eq. (7). Fig. 13 shows the SSR calculated when using as input motion the synthetics extracted

from the PW simulation explained in the validation section. Similar results for the PS simulation are not presented due to space limitations.

$$SSR(f) = \sqrt{(EW_{\text{surface}}^2 + NS_{\text{surface}}^2)/(EW_{\text{depth}}^2 + NS_{\text{depth}}^2)} \quad (7)$$

Fig. 13 summarizes results for four cases, the three cases with the best profiles obtained from the inversion (cases 1–3, lines in shades of blue), and one case of the ‘naive’ parametrization, case number 9 (green lines). The red line represents the SSR for a 1-D analysis conducted with the material properties extracted from the SEM3D mesh (which correspond to the real site properties). In both figures, it can be observed that the results of the profiles from inversion cases 1–3 present a difference in the natural period with respect to the real soil period, a difference of around 0.4 s. This difference is mainly due to a lack of resolution in the MASW test in the low frequencies. The results of case 9, one of the extreme cases of ‘naive’ parametrization, are closer to the 1-D model of the actual site properties. In this case, we defined 25 layers and a V_s variation of 20 per cent. Therefore, we provided input parameters that resemble almost the real solution. In addition, we included the 3-D response obtained in the PW and PS simulations, represented by the black continuous and dashed lines, respectively. As shown in both figures, the 1-D response leads to lower soil frequency and larger amplitudes in the spectral ratio. This behaviour is expected due to the 3-D and 1-D model differences in terms of the material model, 3-D geometry and attenuation.

Additionally, we evaluated the time domain variation of the seismic response in terms of a set of seismic intensity parameters. Due to space limitations, results presented in this article correspond to the peak ground velocity (PGV), the cumulative absolute velocity (CAV) and total duration, which are shown in Fig. 14. Each subplot compares the box plots of the intensities measures per inversion case and motion component (EW, NS and UD). The color is related to each inversion case. The red star depicts the value of the DEEPSOIL 1-D analysis of the material properties extracted from

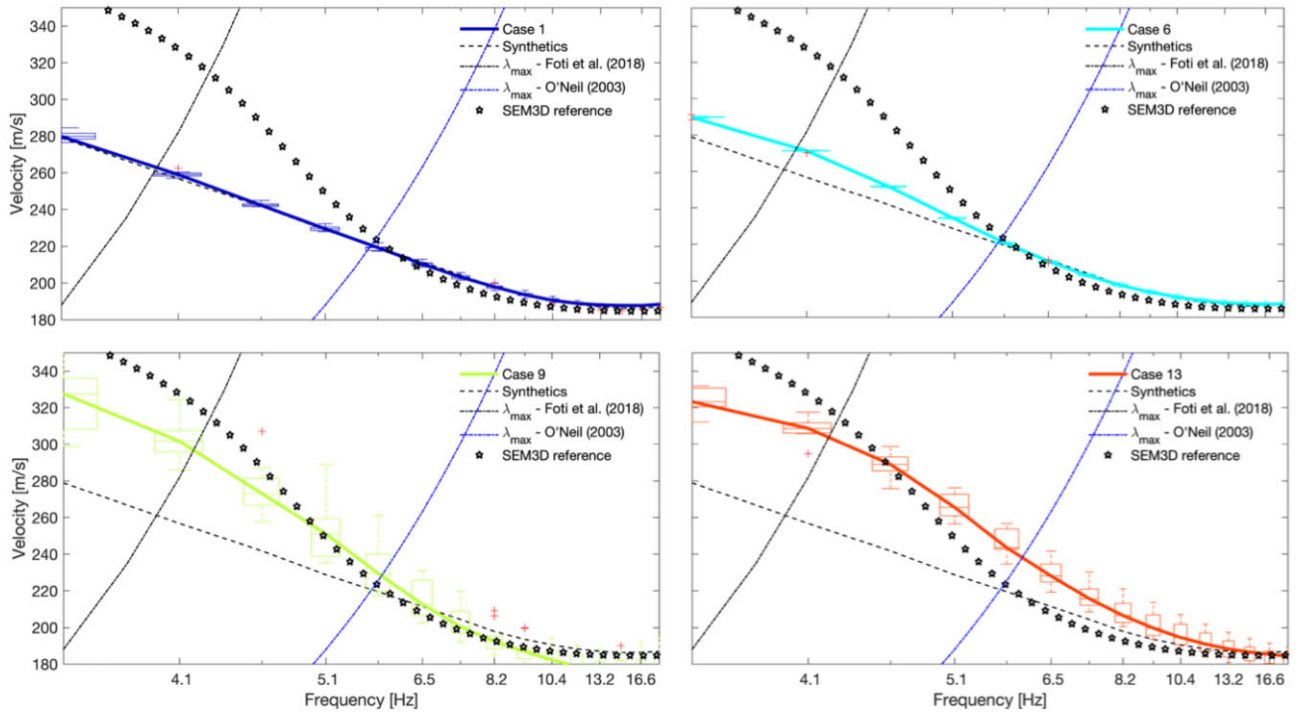


Figure 11. Comparison of the median and boxplots of the dispersion curves corresponding to the 10 ‘best’ soil profiles for inversion cases: 1, 6, 9 and 13.

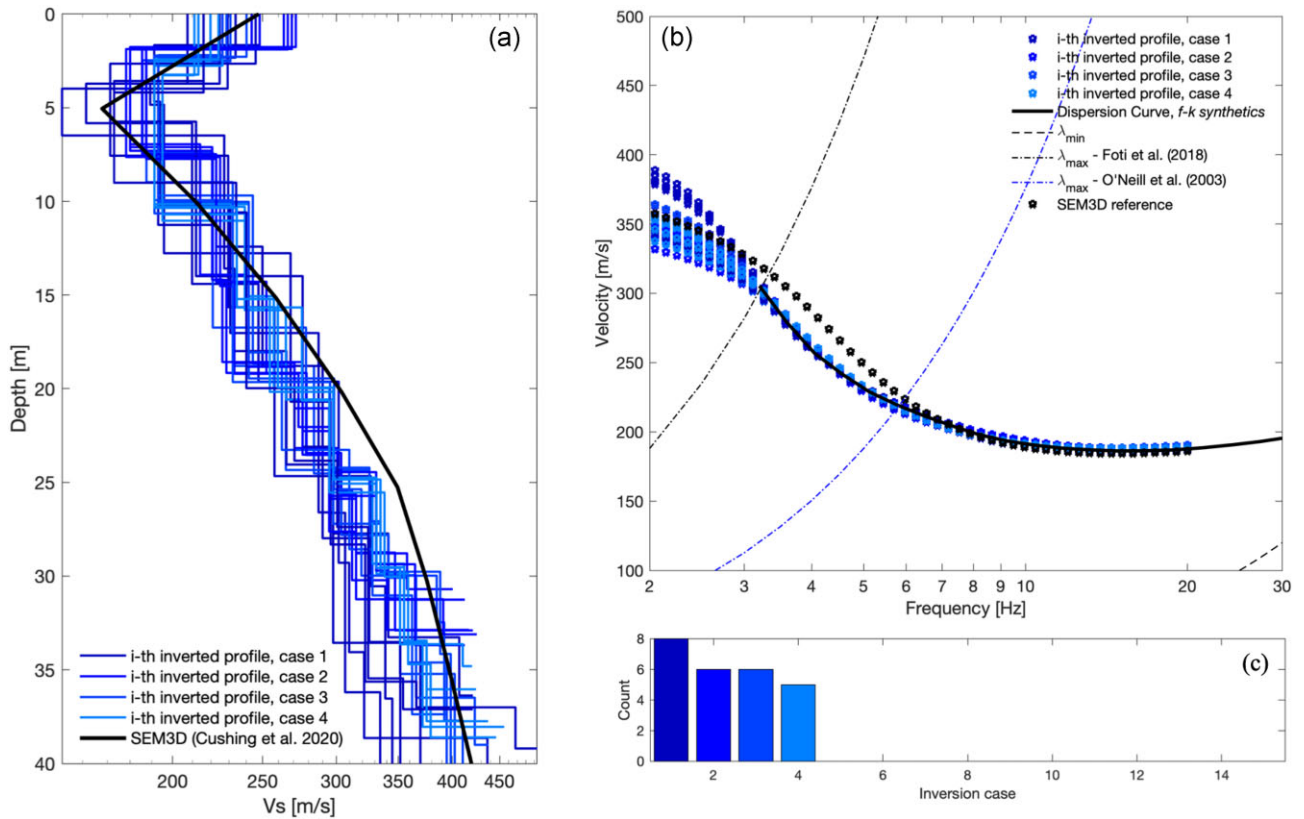


Figure 12. Inversion results, (a) 25 soil profiles with the lowest misfit values among all cases evaluated (b) dispersion curves corresponding to the best 25 soil profiles and (c) histogram showing the distribution per case of the 25 best soil profiles.

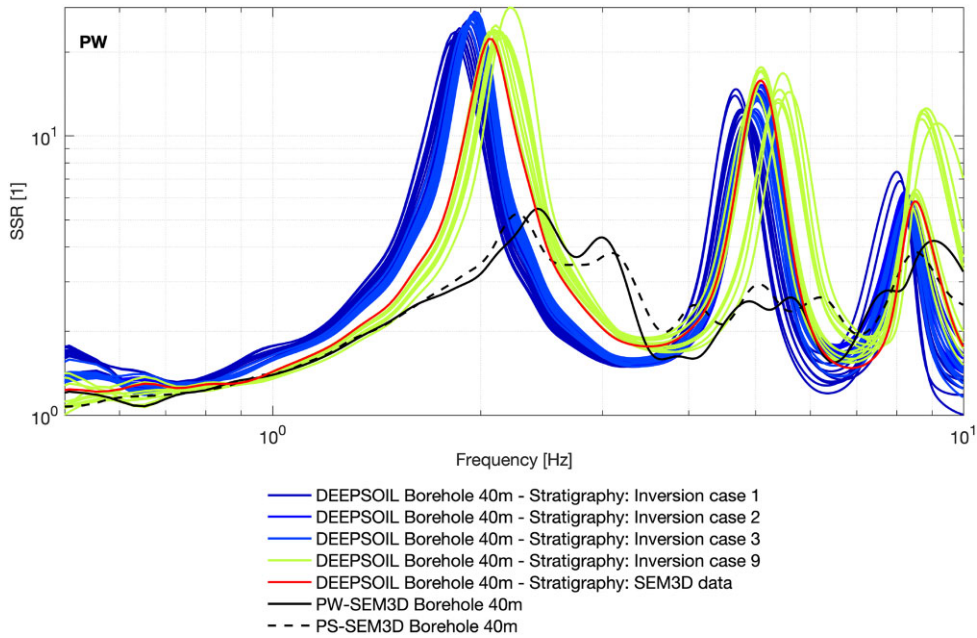


Figure 13. Comparison between spectral ratios. The 1D DEEPSOIL models input motion corresponds to the synthetic of a plane wave propagation conducted in SEM3D registered at the ARGONET coordinates at 40 m depth.

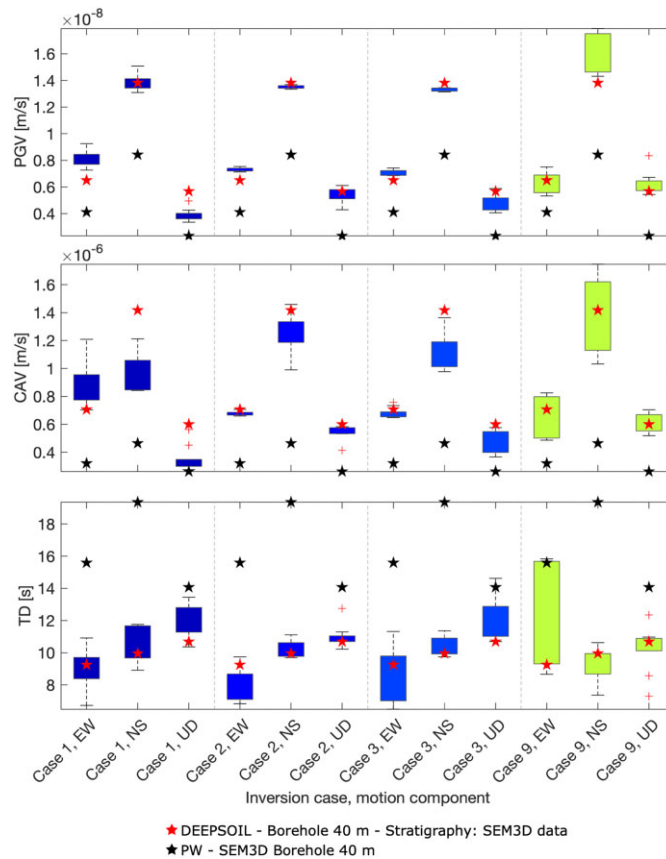


Figure 14. PGV, CAV and TD comparison between 1-D response of inverted and real material properties and 3-D site response.

the 3-D model (reference model), and the black star corresponds to the PW SEM3D simulation results. As shown in Fig. 14, the inverted profiles from cases 1 to 3 led to similar intensities in each motion component when comparing between inversion cases (see,

for instance, NS component for inversion cases 1–3). In general, the results are always close to the 1-D response of the real material properties (red star). The inversion case 9 (‘naive’ parametrization) shows higher dispersion in the response in the three components of

motion. Additionally, compared to the 3-D response, the 1-D analysis leads to an overestimation of the seismic intensities except for the total duration. A result explained by the emergence of surface waves in the 3-D simulation, whose reverberations increase in the duration of the signal. Furthermore, the 1-D analysis of the soil columns from different inversion cases (cases 1–3) led to a similar response in the frequency and time domain. Other parameters such as the arias intensity variation in time could also be assessed to investigate the temporal response even further. Nonetheless, for the set of intensity parameters evaluated, consistent results were obtained. Please note that the goal of results presented in Figs 13 and 14, distinct from evaluating disparities between 3-D and 1-D models using metrics like aggravation factors, is to examine the seismic response of 1-D models derived from the inversion process in comparison to the 3-D ground motion. This comparison allows us to understand how variations in inverted 1-D profiles may impact the 1-D response concerning the natural period and seismic intensities analysed.

5 SIMULATION OF PASSIVE SOURCE TESTS

5.1 Initial condition for the inversion

In the passive source testing, ambient noise is recorded. This type of survey allows the measurement of the dispersion curve from low to intermediate frequencies and depends on factors such as the source location relative to the survey, the velocity structure of the site and the acquisition parameters (Foti *et al.* 2018). In this study, a 3-D simulation was conducted for the region of Argostoli to simulate a passive source test. The selection of the initial condition for the inversion was based on the results obtained in the MASW section. The previous section shows that the lower misfit values were obtained for the parameters defined in the inversion case 1. In this section, we used similar parameters as those described in inversion case 1. Only the depth range was modified to consider depths ranging from 5 to 15 m per layer. To summarize, there are four inversion cases, corresponding to a combination of the each radius and the parameters presented in Table 7.

5.2 Acquisition layout

The guidelines by Foti *et al.* (2018) were followed to define the array geometry. The maximum wavelength is related to the distance between receivers. Hence, the maximum distance between receivers is related as well to the exploration depth. According to Foti *et al.* (2018), the maximum array aperture should be at least equal to one to two times the desired investigation depth. In their study, the authors also recommend combining passive surveys with active surveys to increase the resolution of the layers near the surface. This recommendation deals with the difficulty of obtaining short enough wavelengths from passive surveys. In this study, a set of circular arrays with radius of 10, 20, 30 and 40 m were analysed (the maximum distance between receivers is 20, 40, 60 and 80 m, respectively). In each circular array, nine receivers were set in a circular array plus one receiver in the centre of each array to simulate similar conditions to those used on the field (usually, 8–10 sensors are used on the field). In terms of the time window, usually long duration recording are used. This recordings are divided in shorter windows for the analysis.

5.3 Simulation parameters





The mesh and material properties are the same defined for the active source simulation (MASW). The difference between both cases is mainly in the definition of the source and the acquisition layout (see Fig. 15). Table 8 summarizes the domain sizes and material properties used. In this study, the sources for the passive source test were represented as a set of body forces, following the approach outlined by Bonnefoy-Claudet *et al.* (2004). The algorithm RAN-SOURCE (Moczo *et al.* 2002) was used to model the source. The algorithm creates random sources on the surface or near the surface of a specific domain. The time function is modelled as delta type or pseudo-monochromatic, which are generated to resemble the most common noise sources (impact and pseudo-harmonic) by randomly choosing their length and eigenfrequency (Papadopoulos *et al.* 2013). Specifically, these forces were characterized by randomly distributed directions, amplitudes and source time functions. We used a total of 179 such sources, each defined in both horizontal (X and Y) and vertical (Z) directions. The time evolution of these source forces is depicted in the left column of Fig. 16, where the color map visually associates the source functions with their respective locations, as shown in the right column. Notably, the sources exhibit random distribution patterns and varied initiation times, as illustrated in the figure.

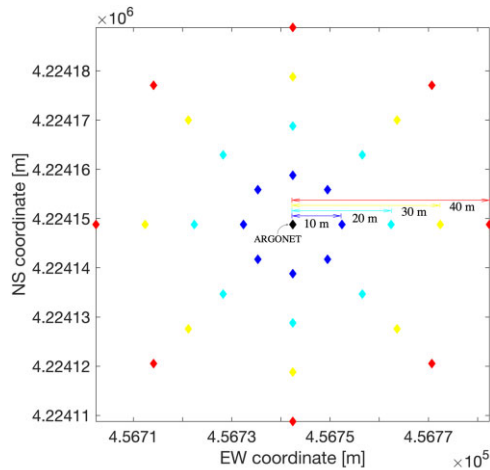
Fig. 17 provides snapshots illustrating the spatial distribution of velocity magnitude on the surface at six discrete time intervals (ranging from 0.1 to 0.6 s). In this figure, the material classification outlined by (Cushing *et al.* 2020) is represented as follows: soft soil materials are denoted by a yellow tone, stiff materials are represented in a blue hue and rock material is distinguished by pink color. Throughout the initial 6-s simulation period, the temporal evolution showcases the emergence of point sources originating at different locations and times within and proximate to the basin. This temporal progression facilitates the modelling of ambient noise phenomena.

5.4 Results

To process the passive source test data, we utilized the GEOPSY MSPAC and SPAC2DISP toolboxes. Specifically, we used the GEOPSY MSPAC toolbox, a versatile software package designed to simplify the process of defining rings from co-array sensor maps. This toolbox allows for the selection of appropriate time limits and signal segments, as well as the configuration of frequency bands and sampling scales for processing. These settings are easily adjustable to accommodate the specific requirements of the user. Once the desired parameters are configured, the computation can be initiated, and the resulting spatial autocorrelation coefficients and computation parameters are saved in a ‘*.target’ file for future use in spac2disp. The spac2disp tool is used to identify the spatial autocorrelation coefficients that contribute most effectively to the dispersion curve. This selection process involves a series of steps, including the selection of minimum and maximum wavenumbers, as well as lower and upper slowness bands. The wavelength limits were determined using the WaranGPS software, which calculates these limits based on the 2-D array configuration. Subsequently, with the SPAC dispersion target defined, we combined the dispersion data from $f - k$ and SPAC using DINVER to conduct the inversion. To enhance the resolution of our results, we included the dispersion curve obtained from the active source simulation as a target, thus integrating data from both active and passive surveys simulated in the Argostoli region. In Fig. 18(a), we present a set of 100 stratigraphies obtained using DINVER. Following a procedure similar to that outlined in the

Table 7. Summary of the input parameters per inversion case. The color code is related to results presented in the following section.

| Color | Case | Radio [m] | N layers | Max. layer thickness [m] | V_s range | Criteria |
|---|------|-----------|------------|-----------------------------|-------------|---------------------|
|  | 1 | 10 | 9 | [5 15 15 15 15 15 15 15 15] | 20 per cent | Geotechnical layers |
|  | 2 | 20 | 9 | [5 15 15 15 15 15 15 15 15] | 20 per cent | Geotechnical layers |
|  | 3 | 30 | 9 | [5 15 15 15 15 15 15 15 15] | 20 per cent | Geotechnical layers |
|  | 4 | 40 | 9 | [5 15 15 15 15 15 15 15 15] | 20 per cent | Geotechnical layers |

**Figure 15.** Acquisition layout.

active source test section, we selected the ten most favourable soil profiles per inversion case based on lower misfit values. Fig. 18(b) illustrates the corresponding dispersion curves.

Combining both passive and active techniques leads to soil profiles with dispersion curves that closely resemble the reference dispersion. As depicted in Fig. 19, we observe a noticeable improvement in the match between dispersion curves and the active-source target curve, particularly within the frequency range of 3–8 Hz. This outcome aligns with prior research, which consistently indicates that active source tests offer higher resolution at higher frequencies, whereas passive source tests improve resolution at lower frequencies. However, it's important to note that the differences between the curves tend to grow for frequencies exceeding 6 Hz when we integrate data from both active and passive source surveys in DINVER. Nevertheless, this combined approach results in profiles that more better represent the properties of the study site and improves depth resolution. The most accurate profiles are derived from data sets created using sensor arrays with radius of 20, 30 and 40 m. This outcome is as anticipated, given that an array with a 10-m radius typically provides resolution only up to approximately 20 m depth. When we compare our findings with those from the active source tests, we find that shear-wave velocity values at depth tend to closely approximate the theoretical profile. Conversely, MASW results often underestimate shear-wave velocity at depth, an observation primarily attributed to the limited resolution of the active source method, particularly at lower frequencies. In future research, we plan to investigate the combined influence of the source model and the study of both Rayleigh and Love waves on resolution and inversion outcomes. This expanded scope will provide a more comprehensive understanding of these factors' effects on our results.

The seismic response of the inverted profiles was analysed to understand the effect of the non-uniqueness of the inversion. To

that end, we computed the seismic response of the profiles obtained from inversion cases 2, 3 and 4. We analysed it in terms of the spectral soil ratio (see Fig. 20) and a series of seismic intensities (see Fig. 21). SSR results for the plane wave input motion are shown in Fig. 20. In this figure, the purple line represents the 1-D response of the site with the material properties used in SEM3D (calculated in DEEPSOIL). The continuous black line depicts the SSR results obtained in the 3-D simulation for the PW propagation, and the black dashed line represents the results for the double-couple point source. As shown in Fig. 20, the 1-D site response of the inverted models tends to have a similar natural frequency and amplitude. This observation remains for the three inversion cases (radius of 20, 30 and 40 m). A slight difference in the fundamental frequency is observed when comparing the 1-D results of the inverted soil columns and the 1-D model of the real site properties (material extracted from the 3-D simulation). However, this difference in frequency is around 0.1, unlike the results obtained in MASW. In that case, generally, the models' frequency difference was about 0.4 seconds and with a higher dispersion between models. Compared to the 3-D results, the 1-D modelling does not accurately reproduce the transfer functions' natural frequency, shape and amplitude of the study site. In addition to the differences between the 3-D and 1-D approaches, this is also due to the material properties at the borehole level (40 m). At this location, the material in the 3-D model has a velocity of 400 m s^{-1} . However, as shown in Section 4, the 1-D response does not adequately represent the 3-D site response, even when the same properties of the 3-D model are considered (material and depth to bedrock). As shown in the results, different layer depths and wave velocity configurations tend to similar site responses, with lower dispersion between inversion cases when combining the passive and active test.

Fig. 21 shows a comparison between seismic intensities (SI) resulting from the 1-D models of the 'best' soil profiles obtained from inversion, the 1-D model of the 'real' material and the 3-D simulation results. The SI presented correspond to the peak ground velocity (PGV), the cumulative absolute velocity (CAV) and total duration (TD). Each 1-D soil profile was analysed in DEEPSOIL, using input motion at the synthetics at the borehole level from two seismic sources: Plane wave propagation and double-couple point source. However, in this article, only results for the PW are presented. In general, the 1-D response shows an overestimation of SI with respect to the 3-D response. Compared to the results obtained from the active survey section, we notice that combining both active and passive surveys results in spectral responses that closely resemble the SSR of the 'real' material in terms of the fundamental period. However, when we examine the time domain results, we observe increased disparities between the 1-D outcomes (inverted profiles) and the actual material properties, particularly when compared to the results derived solely from the active survey data. Specifically, the 1-D models generated from the inversion of active survey data tend to represent better the variations in the 'real'

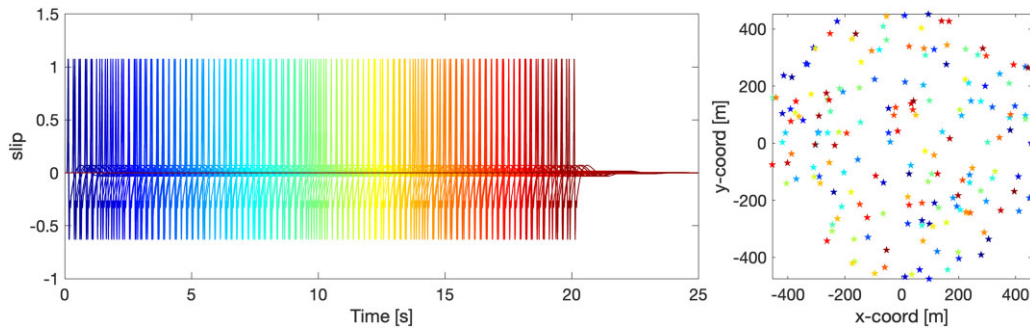


Figure 16. Slip functions and spatial distribution used to simulate the passive source.

Table 8. Summary of the SPAC simulation parameters and computational resources used.

| Parameter | SPAC |
|----------------------------------|--------------------------------|
| Number of processors | 2000 |
| Wave max. freq [Hz] | 30 |
| Min. V_s [m s^{-1}] | 168 |
| Simulation time [s] | 28 |
| Delta time [s] | 1.21E-04 |
| Min element size [m] | 5 |
| Dimension [m] | $8475 \times 8475 \times 2980$ |
| Total wall clock [hh:mm:ss] | 24:00:00 |
| Running time/simulation time | 3085 |

model for layers at depths less than 20 m. However, they tend to underestimate the velocities of layers at depths greater than 20 m. In contrast, the combination of active and passive surveys results in profiles that describe the shallow layers less accurately and tend to overestimate deeper layers' shear wave velocity (V_s). Several factors contribute to these observed differences. First, the discrepancies may be attributed to factors such as mesh resolution and the generation of surface waves. In this case, the simulation domain limits the maximum frequency, potentially affecting the results, especially at higher frequencies. The nature of the seismic source used in our scenario might restrict the generation of such surface waves, contributing to the observed differences. Furthermore, the study conducted by Imtiaz *et al.* (2021) investigated the influence of surface waves diffracted at geological edges within the Argostoli basin, with particular emphasis on higher frequencies. These edge waves' characteristics can vary depending on geological conditions and seismic sources, impacting the dominant types of surface waves recorded in the basin. It is important to note that in this study, our focus was primarily on inverting the fundamental mode of Rayleigh waves. In future research, we intend to explore inversion techniques incorporating Love waves. This approach has the potential to improve result accuracy and offer a more comprehensive insight into site response analysis.

6 DISCUSSION

In this study, a series of simulations were conducted to investigate how well physics-based simulations replicate *in situ* test conditions. We first validated the velocity model for the Argostoli region in Greece and then simulated both active and passive tests. To assess the accuracy of our simulations, we compared spectral ratios at different depths with a bedrock station. Two types of ground motions were generated: one based on plane wave propagation (PW) and the other using a double-couple point source (PS). Our results matched well with those reported by Hollender *et al.* (2018),

particularly regarding spectral soil ratios and natural frequencies. Comparing the simulated and experimental data at various depths, we found that the natural frequency and site response amplitude aligned. However, we observed discrepancies at higher frequencies. Discrepancies observed at higher frequencies are attributed to mesh resolution and the lateral homogeneity of the velocity model that can potentially limit the surface wave phenomena. In addition, previous research has highlighted the influence of edge-diffracted surface waves on the site response in the Argostoli basin, suggesting that this phenomenon may contribute to observed differences with the *in situ* test simulations.

As part of the active test, we performed an active source simulation and used the MASW method. To study the effect of the user defined parameters in the inversion results, we compared dispersion curves for different input parameters cases. We found an improvement in results when input parameters adhered to specific criteria related to layer thicknesses and velocities based on geotechnical data. Moreover, within the context of our simulations, the adherence to the maximum wavelength limit, consistent with O'Neill *et al.* (2003) criterion, proved to establish a more appropriate threshold for our dispersion curves in comparison to the target curve. Our study highlights the importance of defining inversion parameters based on available geophysical data to achieve better alignment with reference curves. We also analysed the seismic response of 1-D models obtained from inversion and calculated soil spectral ratios (SSR) between surface response and borehole data at a depth of 40 m. We noted that disparities in SSR results across different inversion cases were attributable to the limited resolution of the MASW test at lower frequencies, compounded by the reliance solely on profiles selected based on the misfit of dispersion curves. Consequently, for applications like seismic hazard assessment, where the response of the site is heavily influenced by the characterization of shallower soil layers, it is advisable to supplement inversion results with additional *in situ* tests to define parameters such as the natural period of soil vibration.

We used the Spatial Autocorrelation (SPAC) method in the case of the passive test. The results demonstrated that the use of both active and passive survey methods generated dispersion curves and profiles that closely match the reference dispersion curve within the frequency range of 3–8 Hz. This combined approach significantly improved depth resolution, particularly for sensor arrays with radius of 20, 30 and 40 meters. Furthermore, shear-wave velocity values at depth showed a closer match to the theoretical profile when compared to the results from active source tests solely. This improvement in accuracy was consistent across all inversion cases, highlighting the potential benefits of integrating data from both survey methods. Additionally, the examination of seismic response from inverted profiles provided insights into the effectiveness of the SPAC method

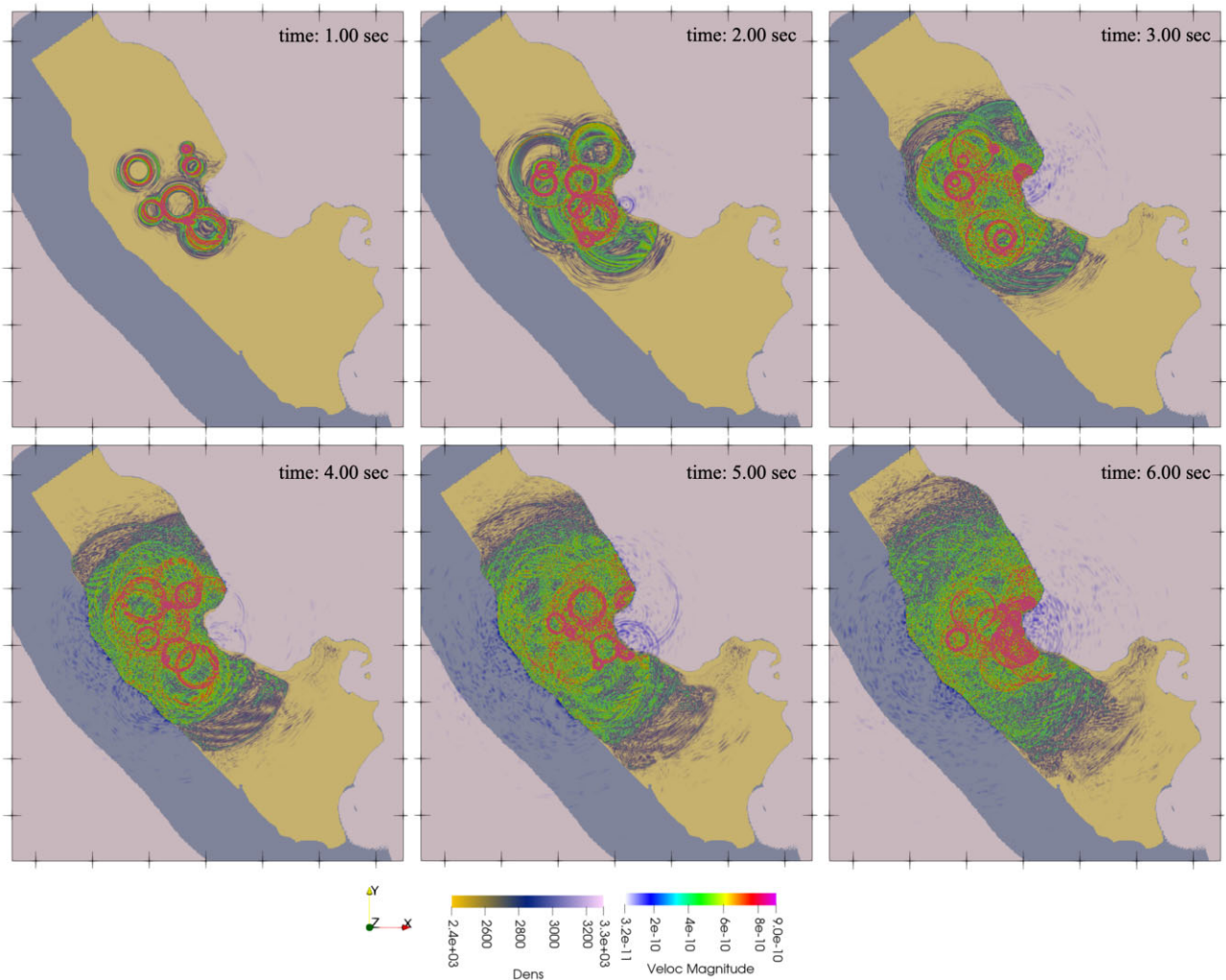


Figure 17. Still-frames of the velocity magnitude on surface for the ambient noise simulation. Corresponding instantaneous times are indicated in each subplot.

in improving resolution at deeper layers, thus contributing to better alignment with the site's natural period. This demonstrates the importance of integrating resolution-enhancing techniques into the inversion process for soil profiles, particularly when the natural period is not explicitly considered during the selection of 1-D profiles for subsequent analysis (e.g. seismic hazard characterization).

Our work has provided valuable insights into the simulation of *in situ* tests and their potential to explore further aspects of variability reported in previous studies (Cornou *et al.* 2006; Tran & Hiltunen 2011; Cox *et al.* 2014; Asten *et al.* 2014; Garofalo *et al.* 2016a, b). However, it is important to acknowledge the inherent limitations. First, our results are subject to the resolution of the mesh and the quality of the input models, which can affect the accuracy of the outcomes. The heterogeneity we observed in our model is mainly due to basin geometry rather than soil properties. This suggests that in the future, it's necessary to integrate spatial variability within the velocity model to address the inherent uncertainties in soil properties. This can be done using advanced methodologies like FWI. However, conducting FWI is beyond the scope of our project. Our aim is to advance the utilization of physics-based simulations using tools like SEM3D and HPC as a virtual laboratory, which allows for testing various configurations in a controlled environment. While sophisticated tools like FWI are available, our goal

is to promote the use of simulations for understanding the sources of variability in inversion results through surface wave analysis, a technique commonly used in engineering and geophysics practice. In our future work, we plan to integrate randomization of the shear wave velocity (V_s) to account for uncertainties in soil properties.

Moreover, we focused on simulating vertical sources for MASW and successfully obtained fundamental modes of Rayleigh waves. However, the use of a vertical force as the active source and the analysis of only the vertical component of motion have limited our consideration of the effect of Love waves. To address this, we plan to explore alternative sources in future work and examine the potential contribution of Love waves to the inversion results. Additionally, the homogeneity of the velocity model may have impacted the effect of higher modes of Rayleigh waves, as only the fundamental mode was observed. Future simulations will consider this factor to enhance the accuracy of our results, taking into account the significant impact of the medium's variability on ground motion, especially at higher frequencies. Finally, our study focused on a single array configuration and source location for the active and passive sources, which may limit the

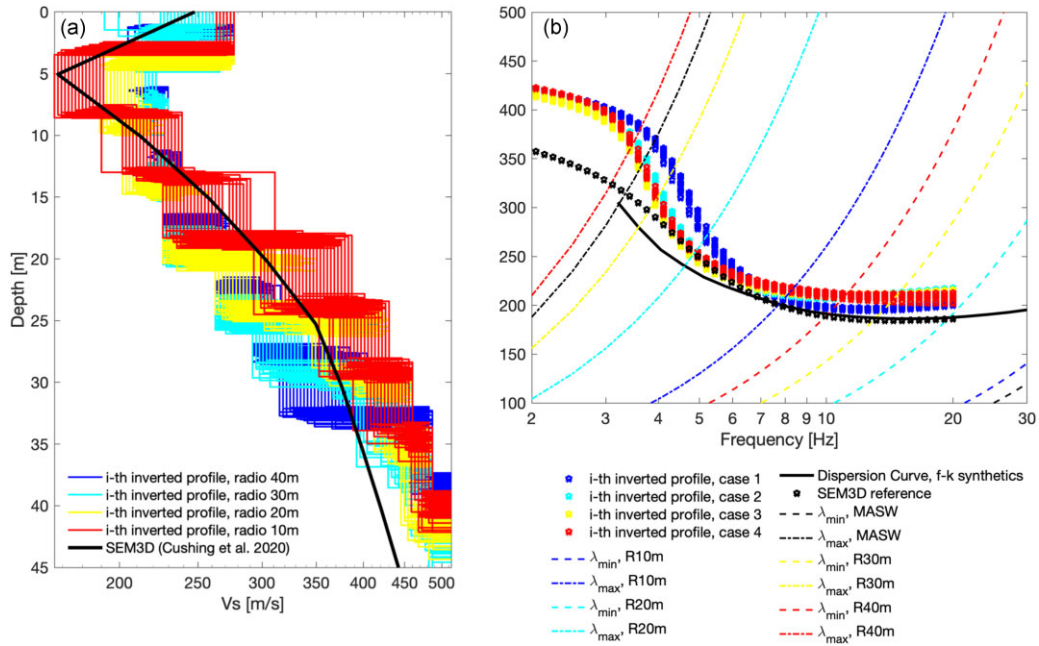


Figure 18. (a) V_s profiles obtained from inversion. The figure shows the 100 best profiles per inversion case based on the misfit calculated by DINVER. (b) Dispersion curves for the ten V_s profiles with lowest misfit per inversion case.

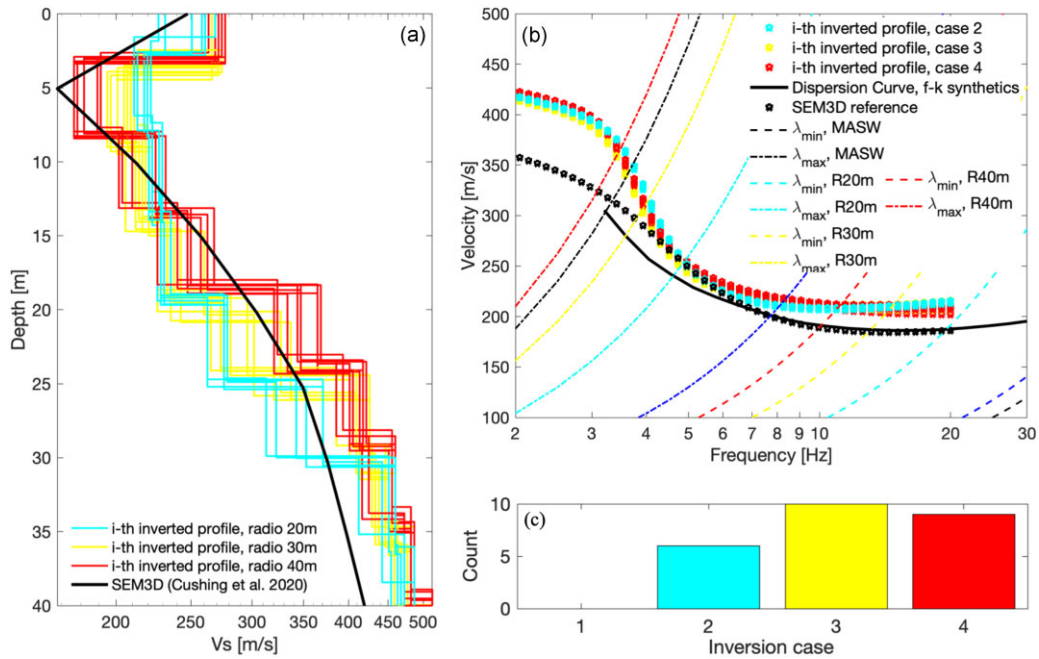


Figure 19. (a) The 25 soil profiles with the lowest misfit values among all cases evaluated, (b) dispersion curves, which are valid only within their corresponding wavelength limits (matching color) and (c) histogram showing the number of profiles within the set of the 25 ‘best’ profiles.

generalization of our findings. To further improve the applicability of our research, future work will include soil heterogeneity, different array configurations and exploring alternative source functions and locations. Nonetheless, the obtained results provide valuable insight and lay the foundation for future research in this area.

7 CONCLUSIONS

The findings of this study demonstrate that physics-based simulations can effectively replicate *in situ* tests. These simulations, performed using SEM3D, offer a promising approach for a thorough evaluation of various geophysical methods, considering both passive and active surveys across diverse scenarios. The virtual

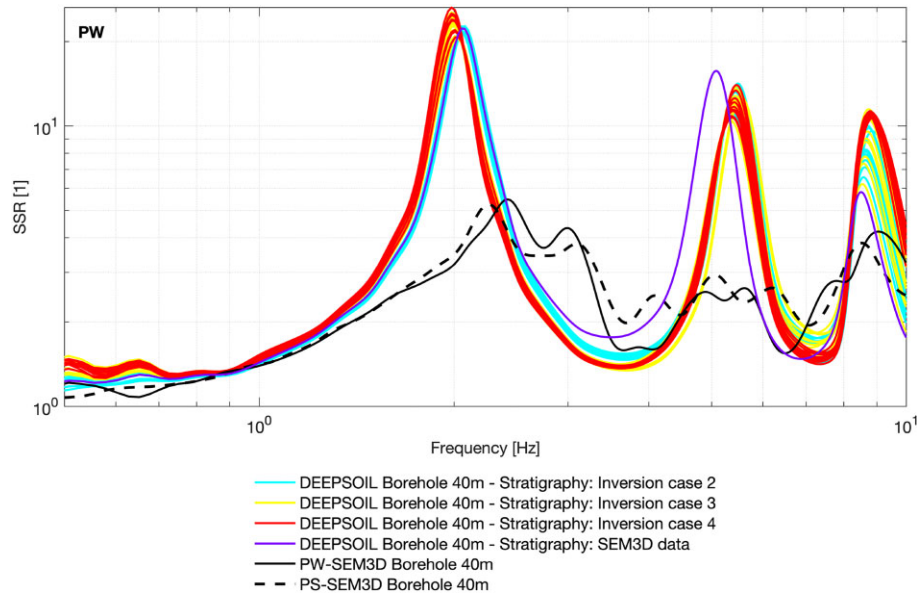


Figure 20. Soil spectral ratios for the best 25 soil profiles and for a input motion at the borehole level extracted from the PW simulation.

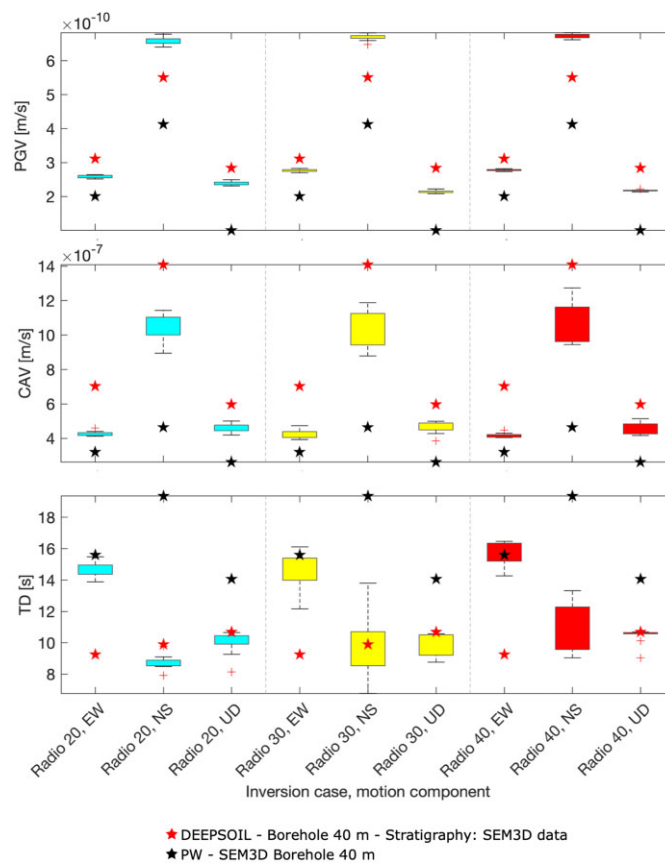


Figure 21. PGV, CAV and TD comparison between 1-D response of inverted and real material properties, and 3-D site response.

laboratory and *in situ* tests were successfully examined and validated for both standard cases and realistic applications in the Argostoli basin. This validation confirms the calibration of the material model and simulation parameters utilized for the study area.

Our study began with the validation of the velocity model for the Argostoli region in Greece, followed by simulations incorporating both active and passive tests. Regarding validation, comparisons with spectral ratios (SSR) revealed favourable agreement with prior studies, particularly regarding SSR amplitudes and

natural frequencies. However, disparities observed at higher frequencies were attributed to limitations in mesh resolution and the lateral homogeneity of the velocity model, potentially constraining the simulation of surface wave phenomena. In the active source simulation, using the MASW's method and analysing the seismic response of the resulting soil profiles allowed observing the impact of input inversion parameter sets determined by two criteria: (i) available geotechnical data and (ii) a naive parametrization. Differences observed in soil spectral ratios highlighted the importance of complementing inversion results with the soil fundamental period, especially for subsequent analyses where the seismic response of shallower soil layers is needed. In the passive source simulation, combining the dispersion curve obtained from the active test with the SPAC technique significantly improved depth resolution, showing the benefit of integrating data from both survey methods. Additionally, analysis of the seismic response of the inverted soil profiles demonstrated the SPAC method's effectiveness in resolving deeper layers, contributing to better alignment with the site's natural period. Finally, an increase in mesh resolution and diversifying input models holds promise for broadening the applicability of our results. While the focus on simulating vertical sources for MASW and the exploration of a single array configuration for both tests, alongside a single location for active and passive sources, provide valuable insights, there remains potential for broadening the scope of our findings. Future efforts will focus on these aspects by examining diverse array configurations and source locations, along with incorporating the inherent variability of soil properties. This systematic approach aims to expand the scope of our research findings.

ACKNOWLEDGMENTS

The research presented in this paper has received support from multiple sources. We acknowledge the contributions of the SIGMA-2 project, funded by EDF (Électricité de France), as well as the SEISME Paris Saclay Research Institute. Furthermore, this work has been made possible through funding from the French National Research Agency (Agence Nationale de la Recherche) within the framework of project ANR Modulate (ANR-18-CE22-0017 - Modelling long-period ground motions and assessment of their effects on large-scale infrastructures). We extend our gratitude to these organizations for their invaluable support, which has played a crucial role in advancing our research.

DATA AVAILABILITY

At this time, we will not be providing access to the data or code. Our simulations involve complex 3-D physics-based modelling, which requires specialized software and computing resources that may not be easily transferable. However, we want to emphasize our commitment to being transparent and conducting our research rigorously. To help others understand and reproduce our work, we have provided a detailed explanation of our methods in this paper. We hope this information will enable researchers with similar resources to replicate our study accurately. We are also open to answering any specific questions about how we conducted our research and what we found. We understand the importance of data and code sharing in advancing scientific knowledge and are actively exploring avenues to make our research more accessible in the future.

REFERENCES

- Aki, K., 1957. Space and time spectra of stationary stochastic waves, with special reference to microtremors, *Bull. Earthq. Res. Inst.*, **35**, 415–456.
- Aki, K., 1965. A note on the use of microseisms in determining the shallow structures of the earth's crust, *Geophysics*, **30**(4), 665–666.
- Askari, R., Ferguson, R.J. & DeMeersman, K., 2011. Estimation of phase and group velocities for multi-modal ground roll using the 'phase shift' and 'slant stack generalized s transform based' methods, *CREWES Res. Rep.*, **23**, 1–11.
- Asten, M.W., Askan, A., Ekinoglu, E.E., Sisman, F.N. & Ugurhan, B., 2014. Site characterisation in north-western turkey based on spac and hvsr analysis of microtremor noise, *Explor. Geophys.*, **45**(2), 74–85.
- Bard, P.-Y. *et al.*, 2010. From non-invasive site characterization to site amplification: recent advances in the use of ambient vibration measurements, in *Earthquake Engineering in Europe. Geotechnical, Geological, and Earthquake Engineering*, Vol. **17**, pp. 105–123, Springer.
- Bonnefoy-Claudet, S., Cornou, C., Kristek, J., Ohrnberger, M., Wathélet, M., Bard, P.-Y., Moczo, P., Fäh, D. & Cotton, F., 2004. Simulation of seismic ambient noise: I. Results of H/V and array techniques on canonical models, in *Proceedings of the 13th World Conference on Earthquake Engineering*, Vancouver, B.C., Canada, 1–6 August 2004.
- Brune, J.N., 1970. Tectonic stress and the spectra of seismic shear waves from earthquakes, *J. geophys. Res.*, **75**(26), 4997–5009.
- CEA, CentraleSupélec, IPGP, and CNRS, 2017. *SEM3D Ver 2017.04 registered at French Agency for Protection of Programs (Dépôt APP)*.
- Cornou, C., Ohrnberger, M., Boore, D.M., Kudo, K., Bard, P.-Y., Chaljub, E., Cotton, F. & Gueguen, P., 2006. Derivation of structural models from ambient vibration array recordings: results from an international blind test, in *Third International Symposium on the Effects of Surface Geology on Seismic Motion (ESG2006)*, Grenoble, France, Vol. **1**, pp. 1127–1215.
- Cox, B., Wood, C. & Teague, D.P., 2014. Synthesis of the utexas1 surface wave dataset blind-analysis study: inter-analyst dispersion and shear wave velocity uncertainty, in *Geo-Congress 2014: Geo-characterization and modeling for sustainability*, pp. 850–859.
- Cushing, E.M., Hollender, F., Moiriat, D., Guyonnet-Benaize, C., Theodoulidis, N., Pons-Branchu, E., Sépulcre, S., Bard, P.-Y., Cornou, C., Dechamp, A. *et al.*, 2020. Building a three dimensional model of the active plio-quaternary basin of Argostoli (Cephalonia Island, Greece): an integrated geophysical and geological approach, *Eng. Geol.*, **265**, doi:10.1016/j.enggeo.2019.105441.
- Fichtner, A., 2010. *Full Seismic Waveform Modelling and Inversion*, Springer Science & Business Media.
- Foti, S. *et al.*, 2018. Guidelines for the good practice of surface wave analysis: a product of the interpacific project, *Bull. Earthq. Eng.*, **16**(6), 2367–2420.
- Garofalo, F. *et al.*, 2016a. Interpacific project: comparison of invasive and non-invasive methods for seismic site characterization. part II: inter-comparison between surface-wave and borehole methods, *Soil Dyn. Earthq. Eng.*, **82**, 241–254.
- Garofalo, F. *et al.*, 2016b. Interpacific project: comparison of invasive and non-invasive methods for seismic site characterization. part I: intra-comparison of surface wave methods, *Soil Dyn. Earthq. Eng.*, **82**, 222–240.
- Gatti, F., 2017. Analyse physics-based de scénarios sismiques de la faille au site: prédiction de mouvement sismique fort pour l'étude de vulnérabilité sismique de structures critiques, *Phd thesis*, Université Paris-Saclay and Politecnico di Milano.
- Hashash, Y., Musgrove, M., Harmon, J., Groholski, D., Phillips, C. & Park, D., 2016. *DEEPSOIL 6.1. User Manual*, Board of Trustees of University of Illinois at Urbana-Champaign.
- Hollender, F., Roumelioti, Z., Régner, J., Perron, V. & Bard, P.-Y., 2018. Respective advantages of surface and downhole reference stations for site effect studies: lessons learnt from the Argonet (Cephalonia Island, Greece) and Cadarache (Provence, France) vertical arrays, in *Proceedings of the 16th European Conference on Earthquake Engineering (16ECEE)*, Thessaloniki, Greece

- Holschneider, M., Diallo, M., Kulesh, M., Ohrnberger, M., Lück, E. & Scherbaum, F., 2005. Characterization of dispersive surface waves using continuous wavelet transforms, *J. geophys. Int.*, **163**(2), 463–478.
- Imtiaz, A., Cornou, C., Bard, P. & Hobiger, M., 2021. Diffracted wavefield decomposition and multidimensional site effects in the Argostoli Valley, Greece, *J. geophys. Int.*, **224**(3), 1849–1869.
- Kulesh, M., Holschneider, M., Diallo, M.S., Xie, Q. & Scherbaum, F., 2005. Modeling of wave dispersion using continuous wavelet transforms, *Pure appl. Geophys.*, **162**, 843–855.
- Loke, M.H., 2004. Tutorial: 2-D and 3-D Electrical Imaging Surveys, Birmingham, UK, <https://www.geotomosoft.com/>.
- Louie, J.N., 2001. Faster, better: shear-wave velocity to 100 meters depth from refraction microtremor arrays, *Bull. seism. Soc. Am.*, **91**(2), 347–364.
- McMechan, G.A. & Yedlin, M.J., 1981. Analysis of dispersive waves by wave field transformation, *Geophysics*, **46**(6), 869–874.
- Moczo, P., Kristek, J., Vavrycuk, V., Archuleta, R.J. & Halada, L., 2002. 3D heterogeneous staggered-grid finite-difference modeling of seismic motion with volume harmonic and arithmetic averaging of elastic moduli and densities, *Bull. seism. Soc. Am.*, **92**(8), 3042–3066.
- Mussett, A.E. & Khan, M.A., 2000. *Looking Into the Earth: an Introduction to Geological Geophysics*, Cambridge Univ. Press.
- Nazarian, S. & Stokoe, K.H., 1984. Nondestructive testing of pavements using surface waves, *Transp. Res. Rec.*, **993**, 67–79.
- O'Neill, A., Dentith, M. & List, R., 2003. Full-waveform P-SV reflectivity inversion of surface waves for shallow engineering applications, *Explor. Geophys.*, **34**(3), 158–173.
- Papadopoulos, I., Papazachos, C., Savvaidis, A., Theodoulidis, N., Valianatos, F. & Tsourlos, P., 2013. Results for the shallow structure of the broader region of Chania by HVSr measurements of ambient noise and their validation using simulation of ambient noise and independent geological information, *Bull. Geol. Soc. Greece*, **47**(3), 1201–1210.
- Park, C.B., Miller, R.D. & Xia, J., 1998. Imaging dispersion curves of surface waves on multi-channel record, in *SEG Technical Program Expanded Abstracts 1998*, pp. 1377–1380, Society of Exploration Geophysicists.
- Park, C.B., Miller, R.D. & Xia, J., 1999. Multichannel analysis of surface waves, *Geophysics*, **64**(3), 800–808.
- Sheriff, R.E. & Geldart, L.P., 1995. *Exploration Seismology*, Cambridge Univ. Press.
- Taborda, R. & Roten, D., 2015. Physics-based ground-motion simulation, in *Encyclopedia of Earthquake Engineering*, Springer-Verlag.
- Tarantola, A., 2005. *Inverse Problem Theory and Methods for Model Parameter Estimation*, SIAM.
- Telford, W.M., Geldart, L.P. & Sheriff, R.E., 1990. *Applied Geophysics*, Cambridge Univ. Press.
- Theodoulidis, N., Hollender, F., Mariscal, A., Moiriat, D., Bard, P.-Y., Konidaris, A., Cushing, M., Konstantinidou, K. & Roumelioti, Z., 2018. The argonet (Greece) seismic observatory: an accelerometric vertical array and its data, *Seismol. Res. Lett.*, **89**(4), 1555–1565.
- Touhami, S., 2019. Numerical modeling of seismic field and soil interaction: application to the sedimentary basin of Argostoli, Greece, *PhD thesis*, Université Paris-Saclay.
- Touhami, S., Gatti, F., Lopez-Caballero, F., Cottéreau, R., de Abreu Corrêa, L., Aubry, L. & Clouteau, D., 2022. SEM3D: a 3D high-fidelity numerical earthquake simulator for broadband (0–10 Hz) seismic response prediction at a regional scale, *Geosciences*, **12**(3), doi:10.3390/geosciences12030112.
- Tran, K.T. & Hiltunen, D.R., 2011. An assessment of surface wave techniques at the Texas A&M National Geotechnical Experimentation Site, in *Geo-Risk 2011: Risk Assessment and Management in Geoengineering*, Geotechnical Special Publication No. 224, pp. 859–866, eds Juang, C. H., Phoon, K. K., Puppala, A. J., Green, R. A. & Fenton, G. A., American Society of Civil Engineers.
- Wathelet, M., Chatelain, J.-L., Cornou, C., Giulio, G.D., Guillier, B., Ohrnberger, M. & Savvaidis, A., 2020. Geopsy: a user-friendly open-source tool set for ambient vibration processing, *Seismol. Res. Lett.*, **91**(3), 1878–1889.
- Wathelet, M., Jongmans, D. & Ohrnberger, M., 2004. Surface-wave inversion using a direct search algorithm and its application to ambient vibration measurements, *Near Surf. Geophys.*, **2**(4), 211–221.
- Xia, J., Miller, R.D. & Park, C.B., 1999. Estimation of near-surface shear-wave velocity by inversion of Rayleigh waves, *Geophysics*, **64**(3), 691–700.
- Yilmaz, O., 1987. *Seismic Data Processing*, Society of Exploration Geophysicists.
- Yilmaz, Ö., 2001. *Seismic Data Analysis*, Vol. 1, Society of Exploration Geophysicists.